Can Science Save the Earth? – Radiation interactions with matter

Alcide Giorgio di Sarra
alcide.disarra@enea.it

IR0000032 – ITINERIS, Italian Integrated Environmental Research Infrastructures System
(D.D. n. 130/2022 - CUP B53C22002150006) Funded by EU - Next Generation EU PNRR-Mission 4 "Education and Research" - Component 2: "From research to business" - Investment 3.1: "Fund for the realisation of an integrated system of research and innovation infrastructures"

Finanziato dall'Unione europea NextGenerationEU
Ministero dell'Università e della Ricerca
Italiadomani

Pierre Bouguer (1698-1758)

Johann Heinrich Lambert
(1728-1777)

August Beer
(1825-1863)

40

Optical depth

$$k = k_a + k_s$$

$$\tau = \tau_a + \tau_s$$

Bouguer/Lamber/Beer law

$$dL_\lambda = -(k_a + k_s) L_\lambda \frac{dz}{cos\theta} = -k\, L_\lambda \frac{dz}{cos\theta}$$

$$cos\theta \frac{dL_\lambda}{L_\lambda} = -d\tau$$

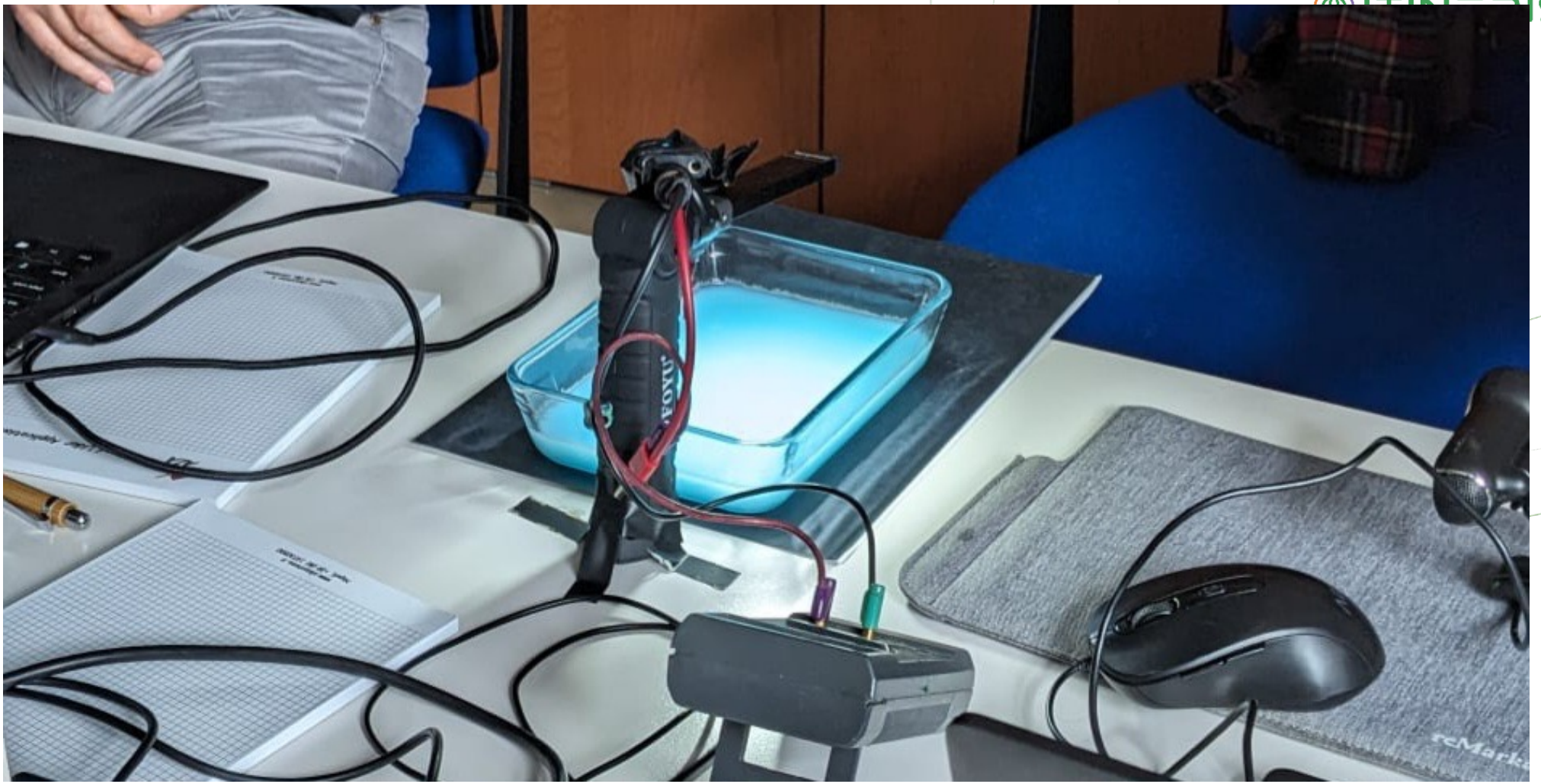
FOYL

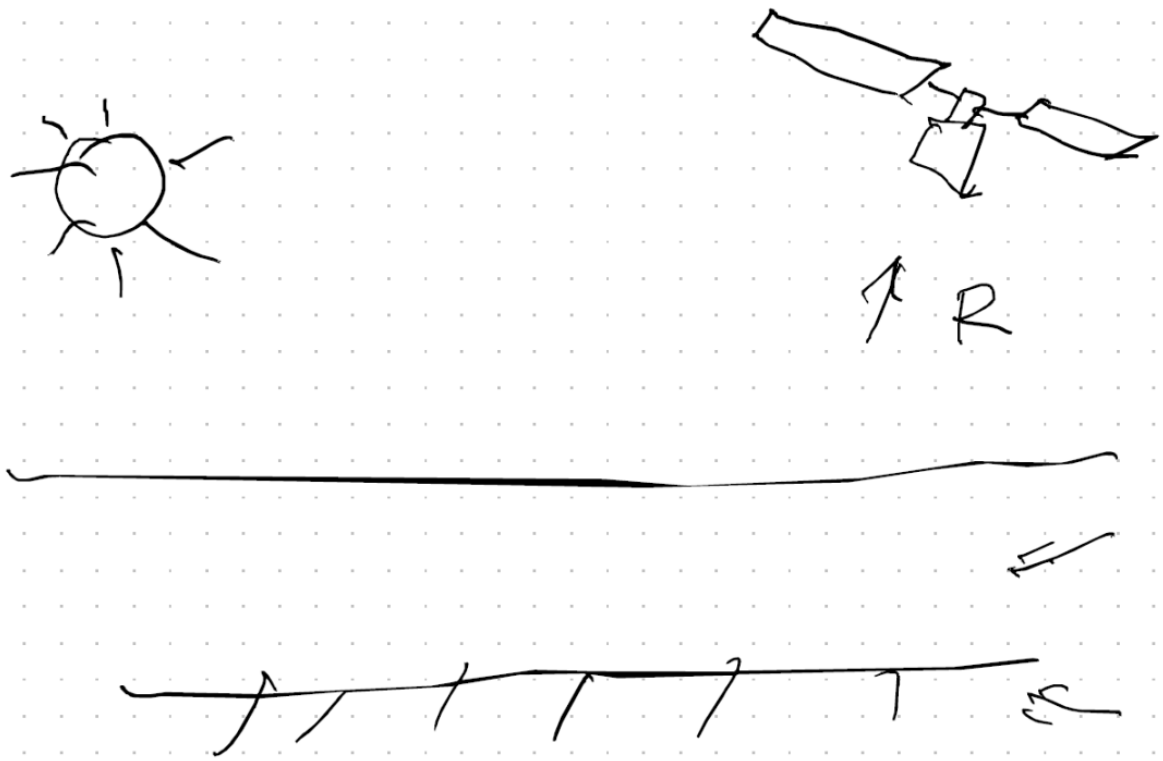
R

P1 Scattering aerosol

P2 absorbing aerosol

HA, P1 $\Delta R \simeq 0$ mV

LA, P1 $\Delta R = -21$ mV

HA, P2 $\Delta R = -[23 - 35] = +12$ mV

LA, P2 $\Delta R = -[20 - 23] = +3$ mV

P1 Scattering aerosol

P2 absorbing aerosol

HA, P1 $\Delta R \simeq 0$ mV

LA, P1 $\Delta R = -21$ mV cooling

HA, P2 $\Delta R = -[23 - 35] = +12$ mV

LA, P2 $\Delta R = -[20 - 23] = +3$ mV warming

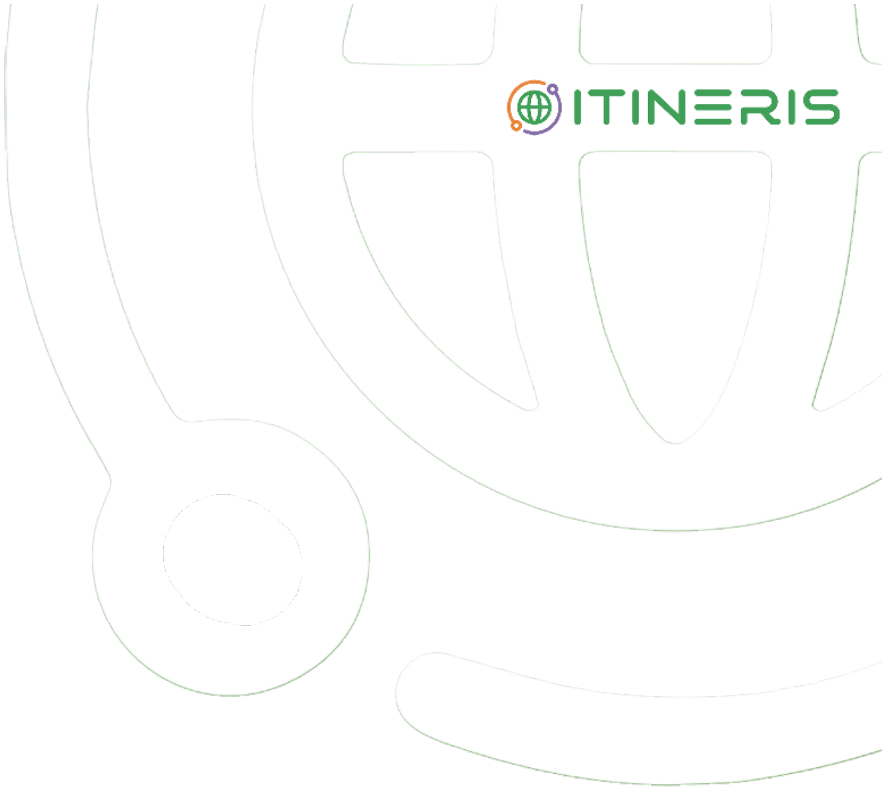
ITINERIS

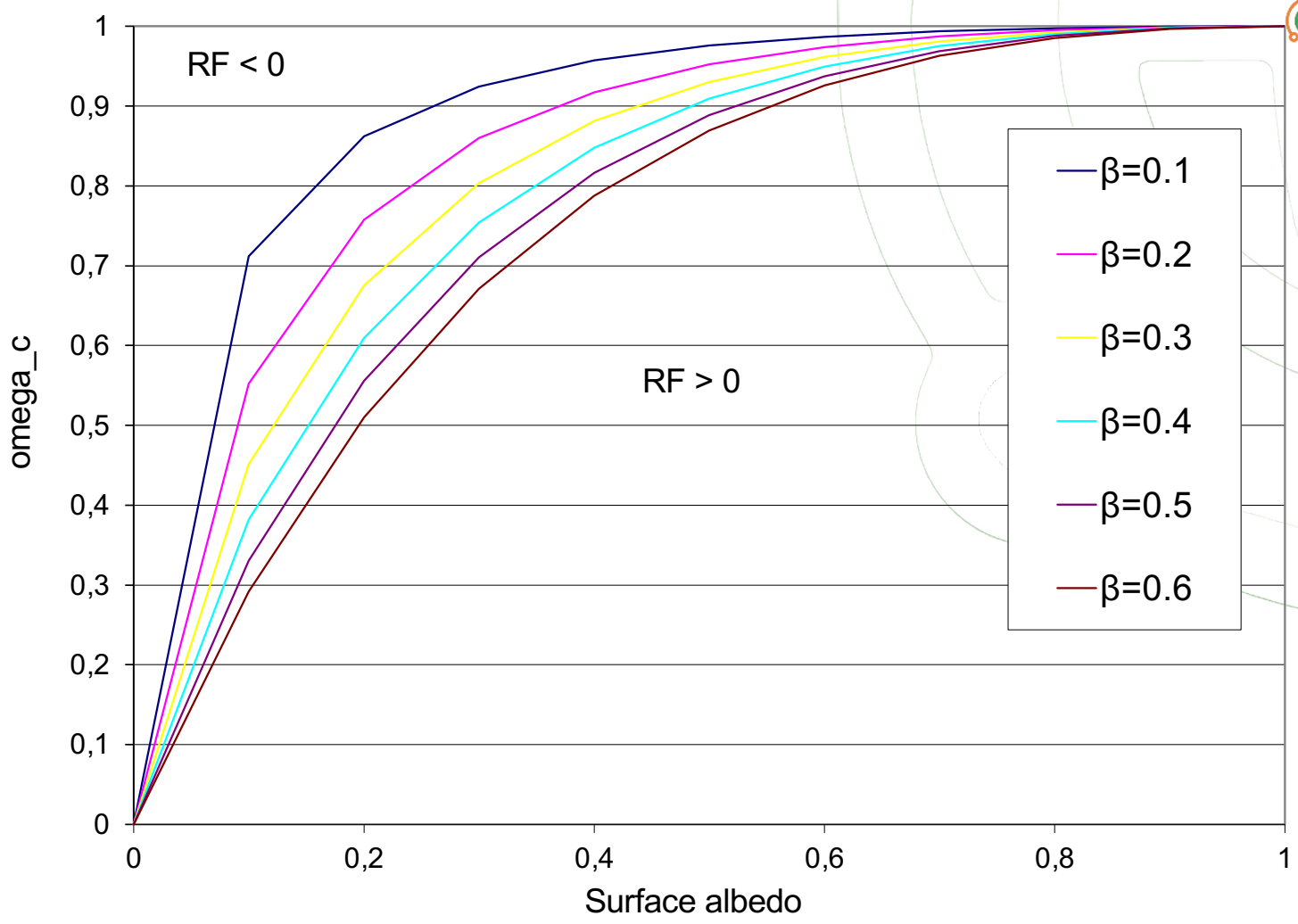
RF < 0
RF > 0
omega_c
Surface albedo
0
0,1
0,2
0,3
0,4
0,5
0,6
0,7
0,8
0,9
1
0,2
0,4
0,6
0,8
β=0.1
β=0.2
β=0.3
β=0.4
β=0.5
β=0.6

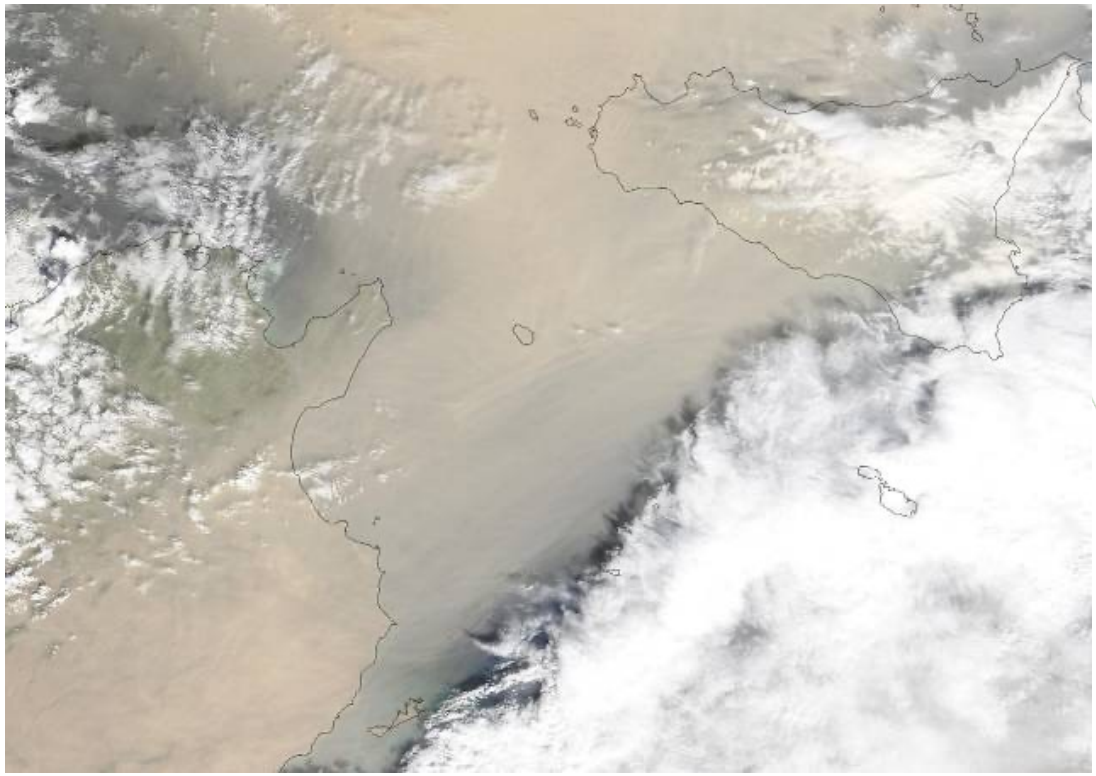

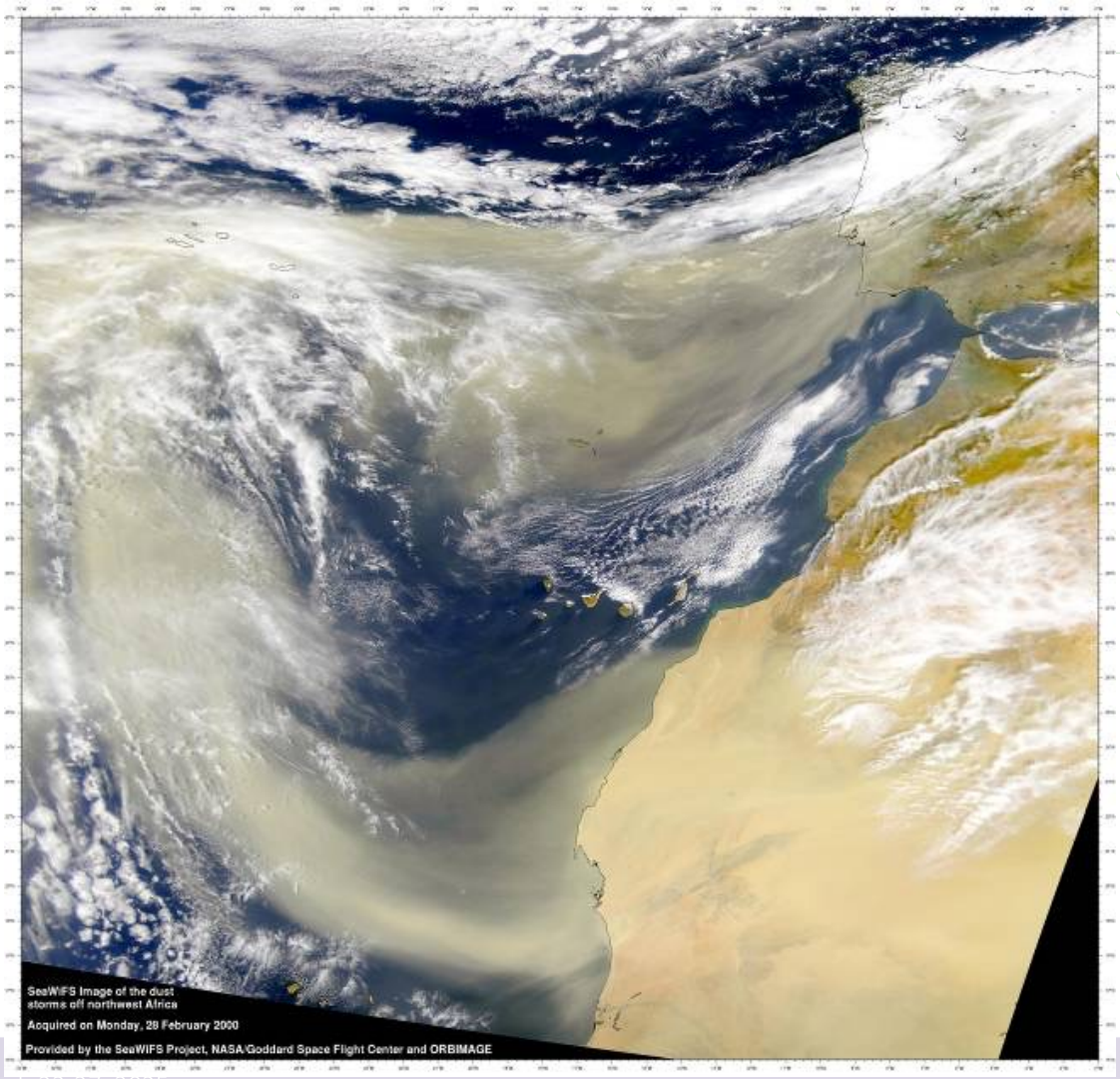
SeaWiFS Image of the dust
storms off northwest Africa
Acquired on Monday, 28 February 2000
Provided by the SeaWiFS Project, NASA/Goddard Space Flight Center and ORBIMAGE


N
Po River
valley
Adriatic Sea

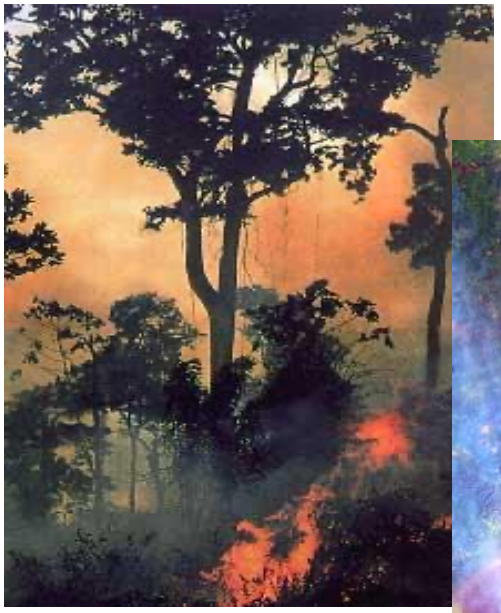

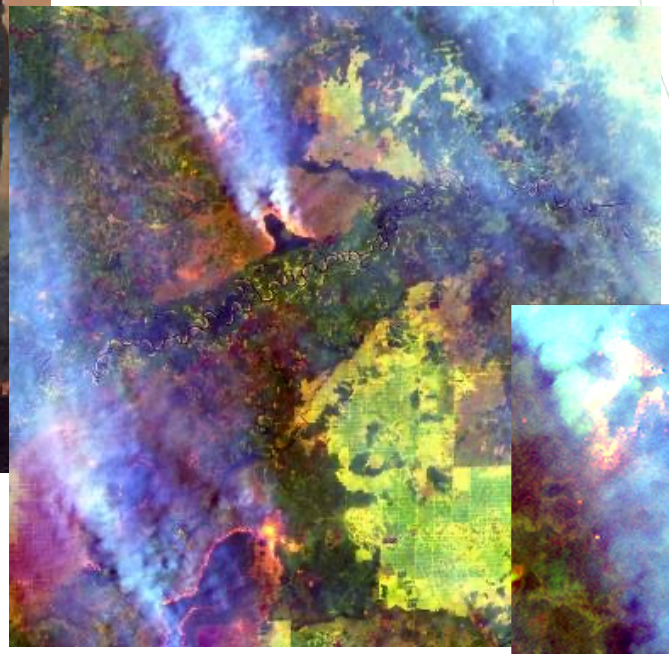

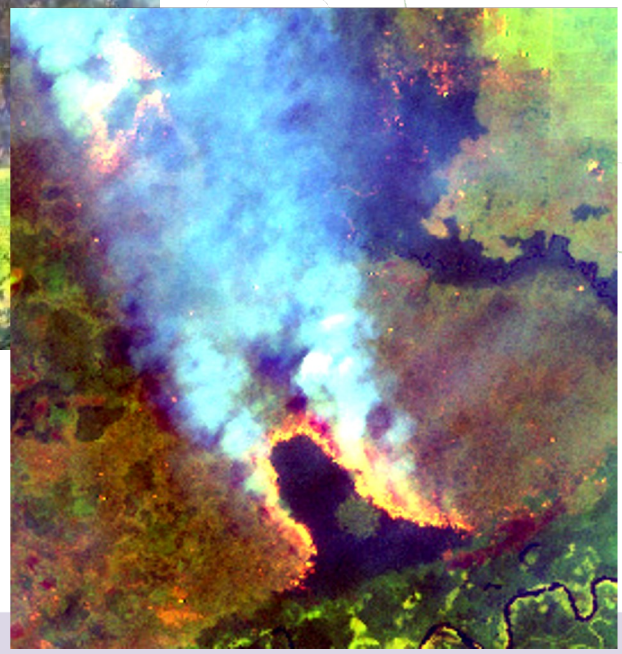

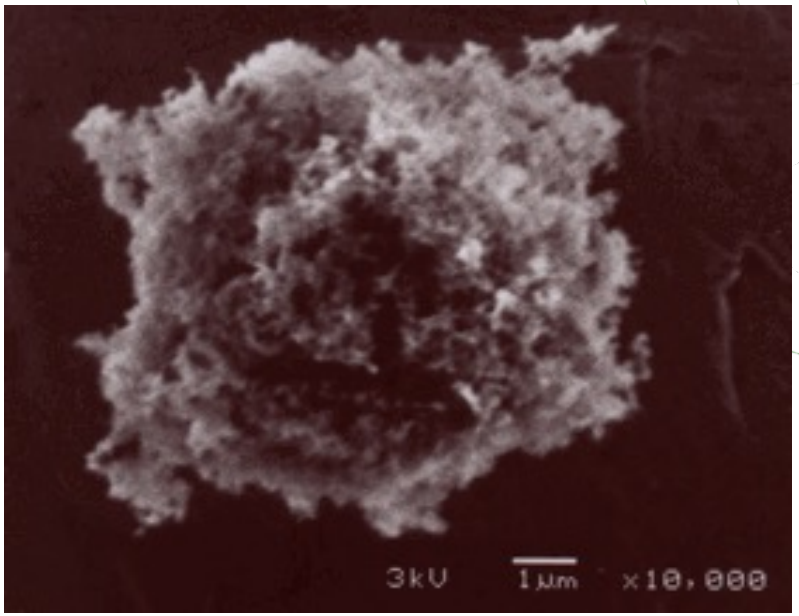
3kV
1µm
x10,000

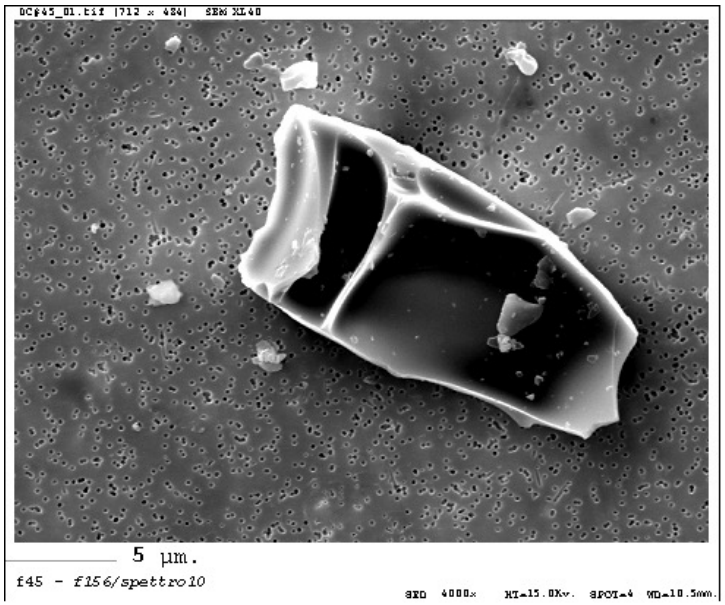
DC$45_01.tif |712 x 484| SEM XL40
5 µm.
f45 - f156/spettro10
SEM 4000x HV=15.0Kv. SPOT=4 WD=10.5mm.

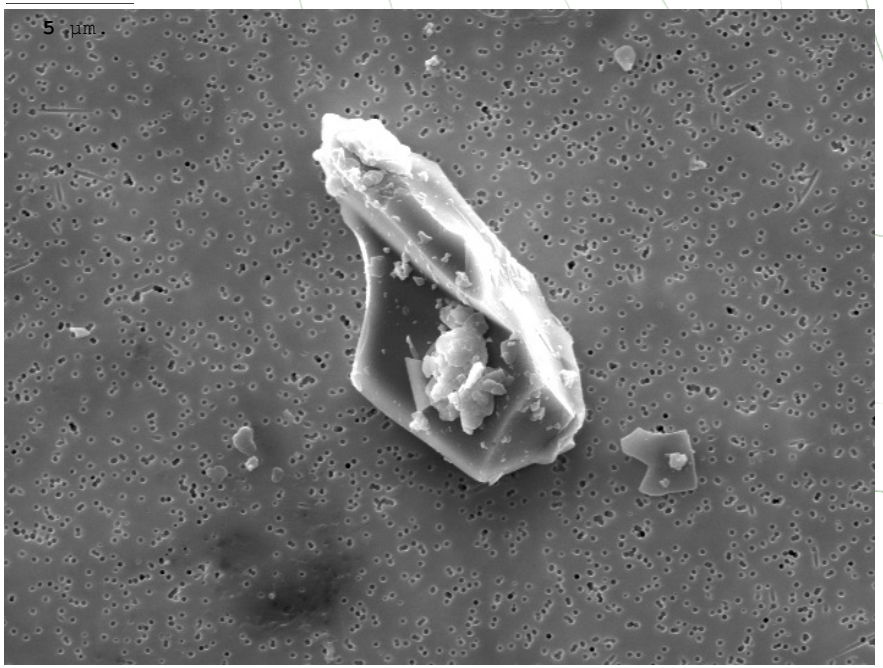
5 µm.

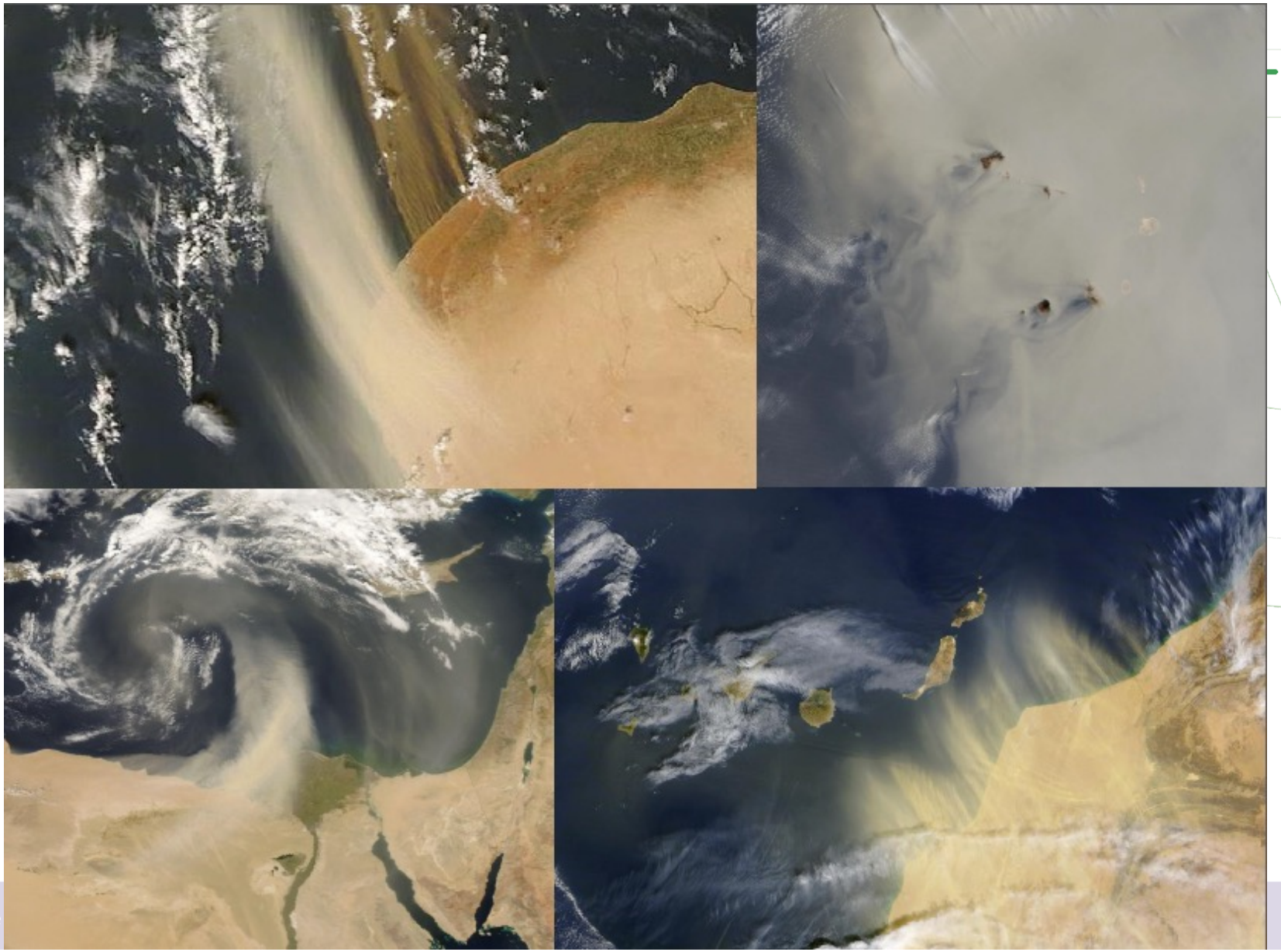

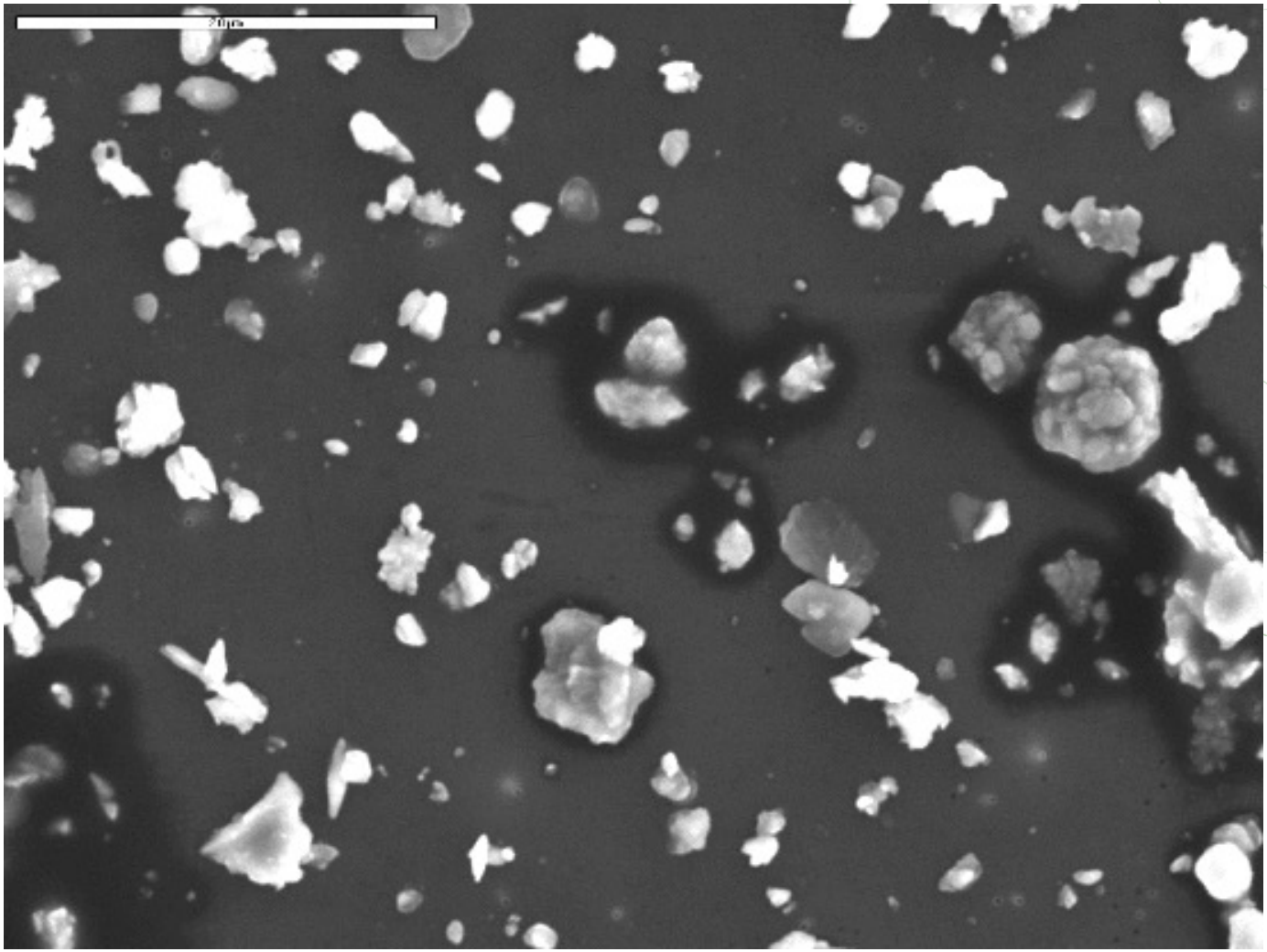

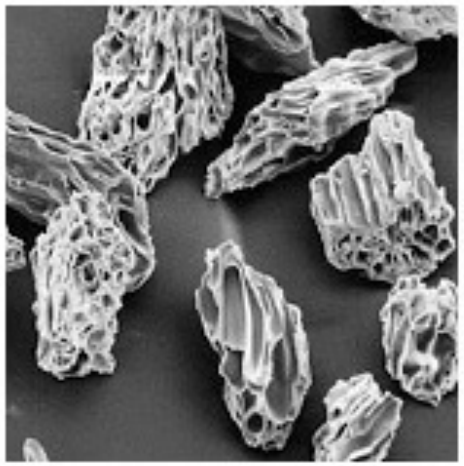

volcanic particles

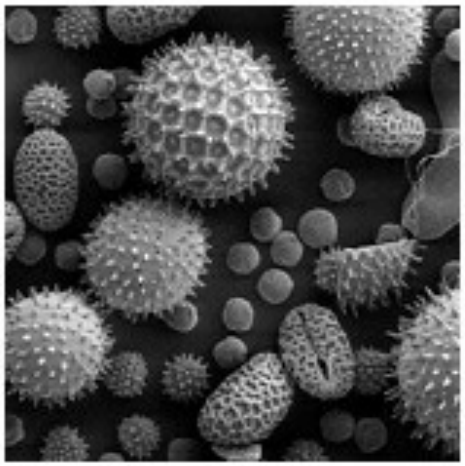

pollen

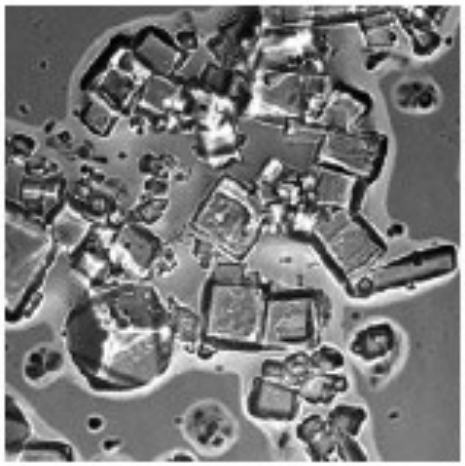

sea salt

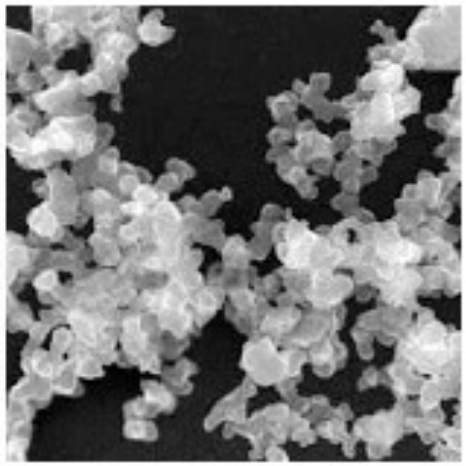

soot

natural

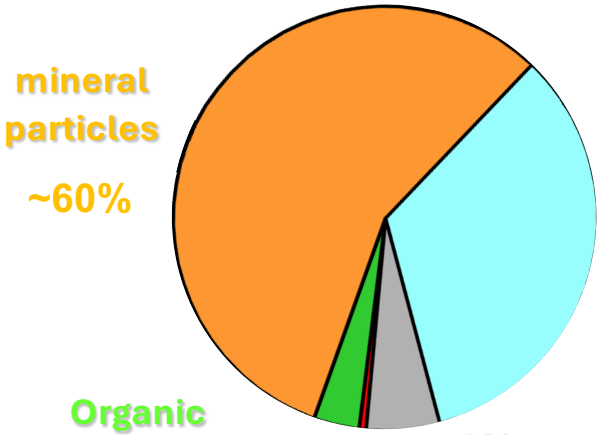

Textor et al., 2006

anthropic

- Primary/secondary particles

- Phase
  - Liquid: droplets, often solution
  - Solid:
    Single / Aggregates
  - Solid/Liquid
    Droplets with solid inclusions
    Aggregates with liquid films

- Mixed
  internally or externally mixed

Table 5.3: Primary particle emissions for the year 2000 (Tg/yr)[a].

	Northern Hemisphere	Southern Hemisphere	Global	Low	High	Source
Carbonaceous aerosols						
Organic Matter (0–2 µm)						
Biomass burning	28	26	54	45	80	Liousse *et al.* (1996), Scholes and Andreae (2000)
Fossil fuel	28	0.4	28	10	30	Cook *et al.* (1999), Penner *et al.* (1993)
Biogenic (>1µm)	—	—	56	0	90	Penner (1995)
Black Carbon (0–2 µm)						
Biomass burning	2.9	2.7	5.7	5	9	Liousse *et al.* (1996); Scholes and Andreae (2000)
Fossil fuel	6.5	0.1	6.6	6	8	Cooke *et al.* (1999); Penner *et al.* (1993)
Aircraft	0.005	0.0004	0.006			
Industrial Dust, etc. (> 1 µm)			100	40	130	Wolf and Hidy (1997); Andreae (1995)
Sea Salt						Gong *et al.* (1998)
d< 1 µm	23	31	54	18	100	
d=1–16µm	1,420	1,870	3,290	1,000	6,000	
Total	1,440	1,900	3,340	1,000	6,000	
Mineral (Soil) Dust [b]						
d< 1 µm	90	17	110	—	—	
d=1–2µm	240	50	290	—	—	
d=2–20µm	1,470	282	1,750	—	—	
Total	1,800	349	2,150	1,000	3,000	

[a] Range reflects estimates reported in the literature. The actual range of uncertainty may encompass values larger and smaller than those reported here.
[b] Source inventory prepared by P. Ginoux for the IPCC Model Intercomparison Workshop.

Table 5.2: Annual source strength for present day emissions of aerosol precursors (Tg N, S or C /year). The reference year is indicated in parentheses behind individual sources, where applicable.

	Northern Hemisphere	Southern Hemisphere	Global[a]	Range	Source
NO_x (as TgN/yr)	32	9	41		(see also Chapter 4).
Fossil fuel (1985)	20	1.1	21		Benkovitz *et al.* (1996)
Aircraft (1992)	0.54	0.04	0.58	0.4–0.9	Penner *et al.* (1999b); Daggett *et al.* (1999)
Biomass burning (ca. 1990)	3.3	3.1	6.4	2–12	Liousse *et al.* (1996); Atherton (1996)
Soils (ca. 1990)	3.5	2.0	5.5	3–12	Yienger and Levy (1995)
Agricultural soils			2.2	0–4	"
Natural soils			3.2	3–8	"
Lightning	4.4	2.6	7.0	2–12	Price *et al.* (1997); Lawrence *et al.* (1995)
NH_3 (as TgN/yr)	41	13	54	40–70	Bouwman *et al.* (1997)
Domestic animals (1990)	18	4.1	21.6	10–30	"
Agriculture (1990)	12	1.1	12.6	6–18	"
Human (1990)	2.3	0.3	2.6	1.3–3.9	"
Biomass burning (1990)	3.5	2.2	5.7	3–8	"
Fossil fuel and industry (1990)	0.29	0.01	0.3	0.1–0.5	"
Natural soils (1990)	1.4	1.1	2.4	1–10	"
Wild animals (1990)	0.10	0.02	0.1	0–1	"
Oceans	3.6	4.5	8.2	3–16	"
SO_2 (as TgS/yr)	76	12	88	67–130	
Fossil fuel and industry (1985)	68	8	76	60–100	Benkovitz *et al.* (1996)
Aircraft (1992)	0.06	0.004	0.06	0.03–1.0	Penner *et al.* (1998a); Penner *et al.* (1999b); Fahey *et al.* (1999)
Biomass burning (ca. 1990)	1.2	1.0	2.2	1–6	Spiro *et al.* (1992)
Volcanoes	6.3	3.0	9.3	6–20	Andres and Kasgnoc (1998) (incl. H_2S)
DMS or H_2S (as TgS/yr)	11.6	13.4	25.0	12–42	
Oceans	11	13	24	13–36	Kettle and Andreae (2000)
Land biota and soils	0.6	0.4	1.0	0.4–5.6	Bates *et al.* (1992); Andreae and Jaeschke (1992)
Volatile organic emissions (as TgC/yr)	171	65	236	100–560	
Anthropogenic (1985)	104	5	109	60–160	Piccot *et al.* (1992)
Terpenes (1990)	67	60	127	40–400	Guenther *et al.* (1995)

[a] The global figure may not equal the sum of the N. hemisphere and S. Hemisphere totals due to rounding.

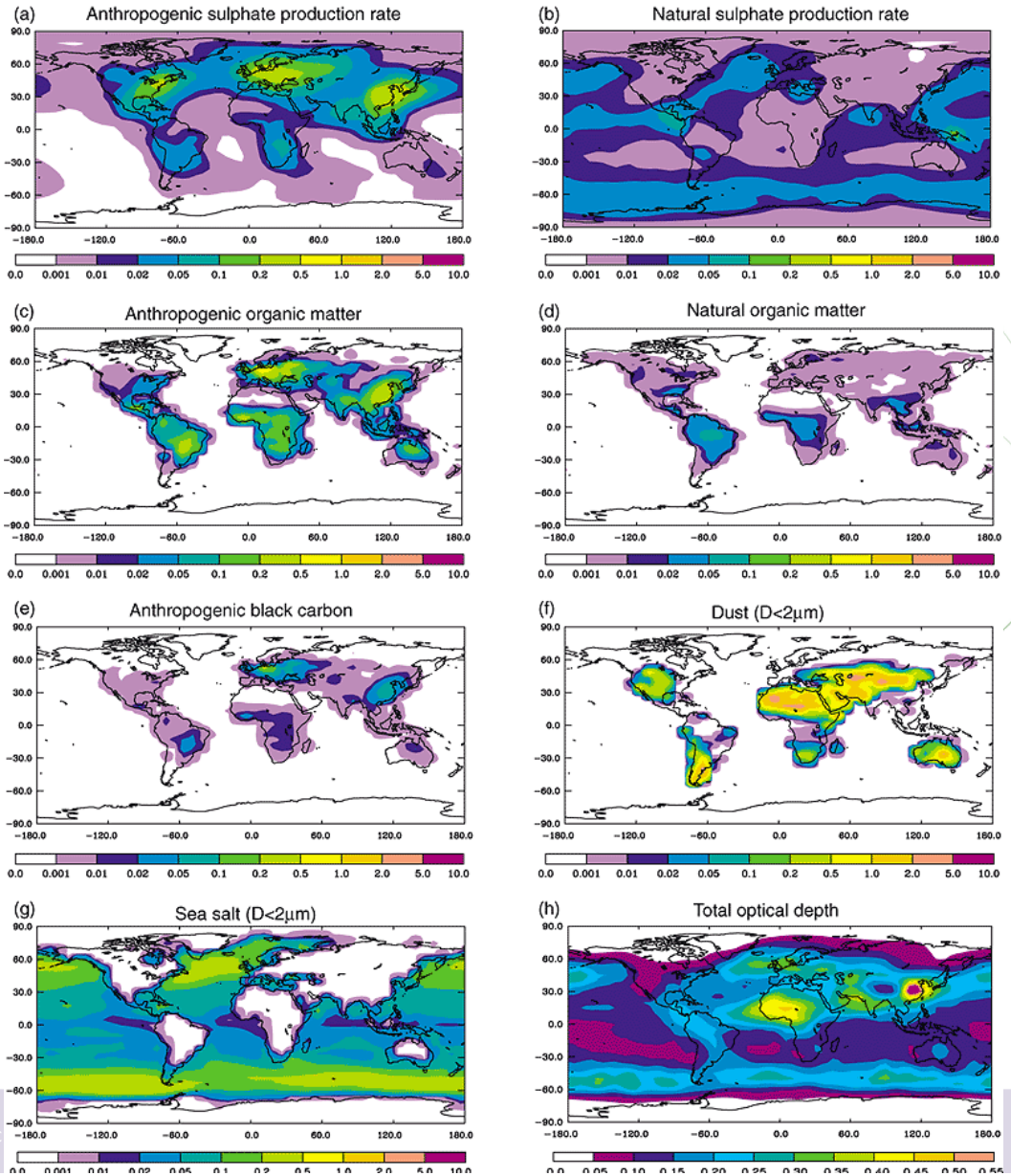
(a) Anthropogenic sulphate production rate
(b) Natural sulphate production rate
(c) Anthropogenic organic matter
(d) Natural organic matter
(e) Anthropogenic black carbon
(f) Dust (D<2μm)
(g) Sea salt (D<2μm)
(h) Total optical depth

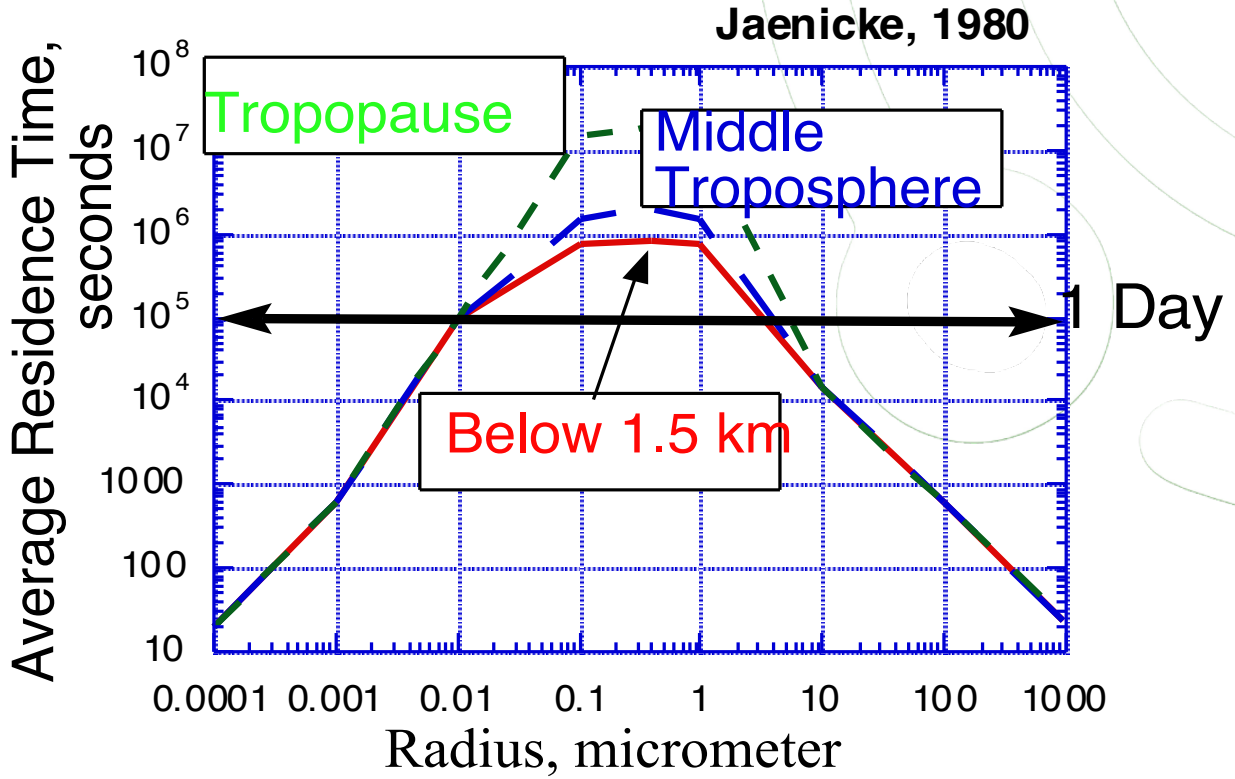
Jaenicke, 1980
Average Residence Time, seconds
10^8
10^7
10^6
10^5
10^4
1000
100
10
Tropopause
Middle Troposphere
1 Day
Below 1.5 km
0.0001
0.001
0.01
0.1
1
10
100
1000
Radius, micrometer

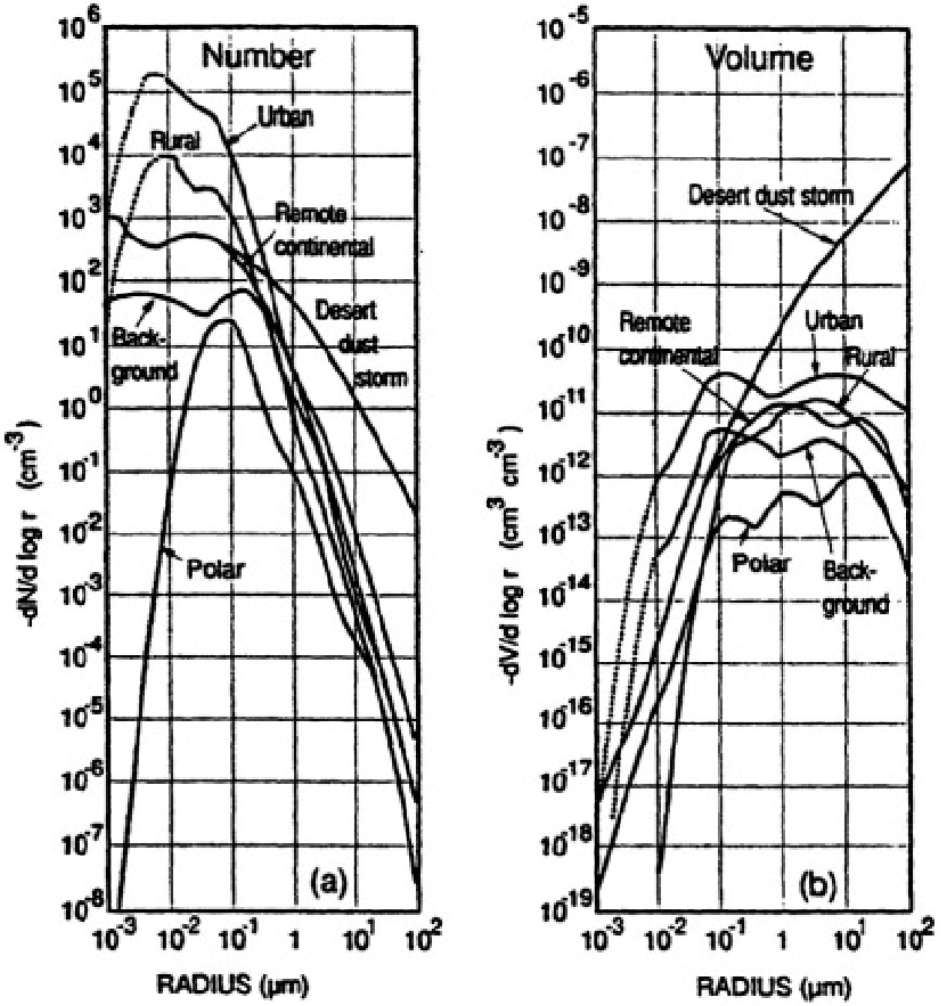
Number
Urban
Rural
Remote continental
Desert dust storm
Back-ground
Polar
(a)
-dN/d log r (cm^{-3})
RADIUS (μm)
Volume
Desert dust storm
Remote continental
Urban
Rural
Polar
Back-ground
(b)
-dV/d log r (cm^3 cm^{-3})
RADIUS (μm)

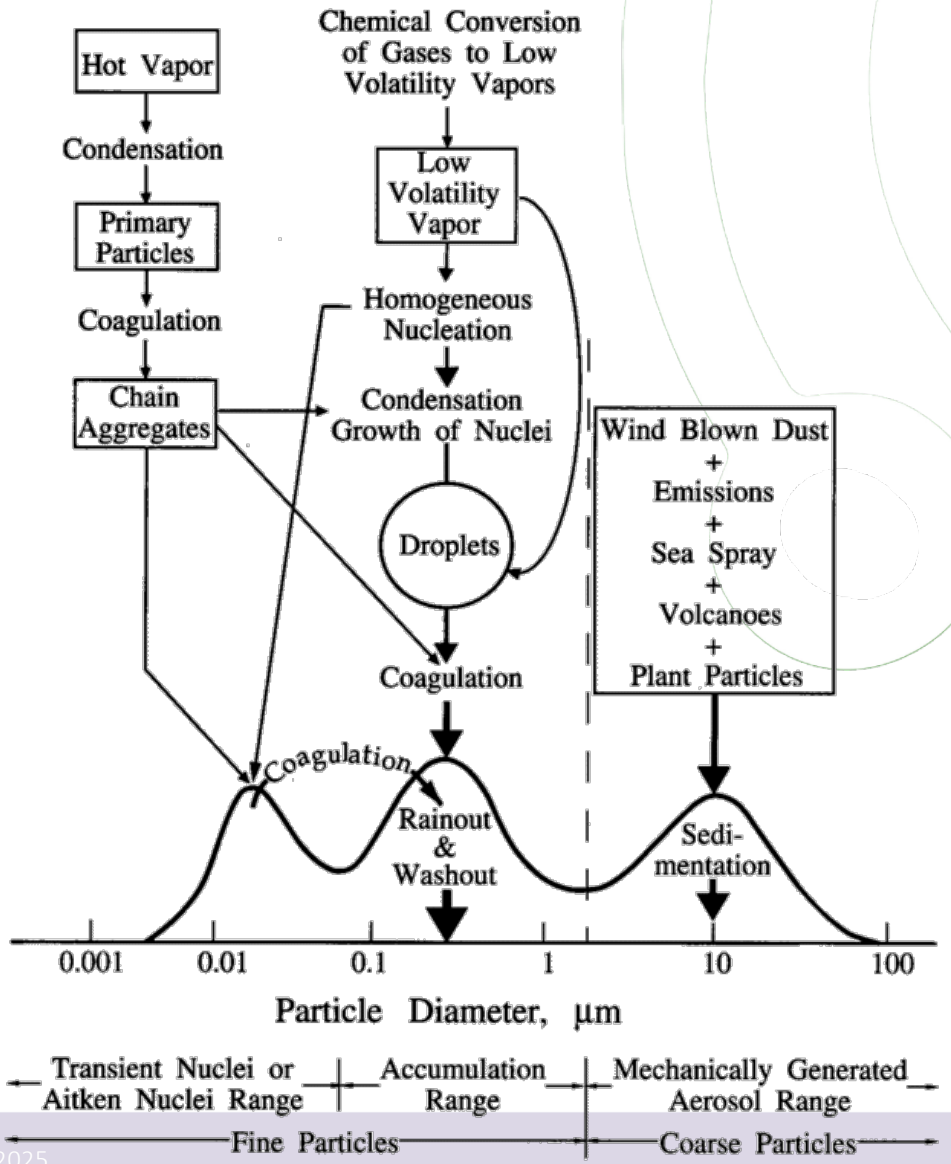
Hot Vapor
Condensation
Primary Particles
Coagulation
Chain Aggregates
Chemical Conversion of Gases to Low Volatility Vapors
Low Volatility Vapor
Homogeneous Nucleation
Condensation Growth of Nuclei
Droplets
Coagulation
Coagulation
Rainout & Washout
Wind Blown Dust + Emissions + Sea Spray + Volcanoes + Plant Particles
Sedi-mentation
0.001
0.01
0.1
1
10
100
Particle Diameter, µm
Transient Nuclei or Aitken Nuclei Range
Accumulation Range
Mechanically Generated Aerosol Range
Fine Particles
Coarse Particles







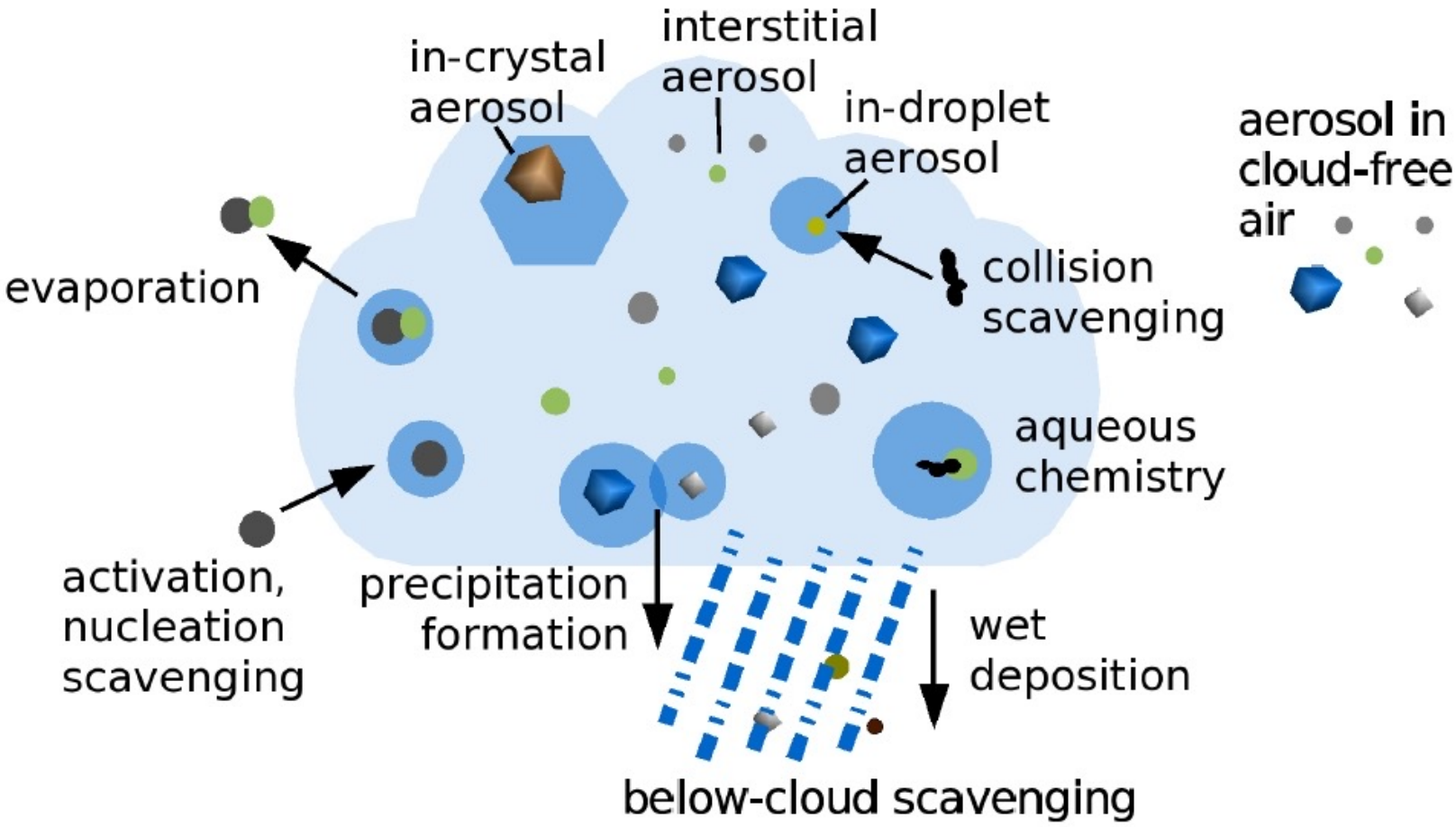
in-crystal aerosol
interstitial aerosol
in-droplet aerosol
aerosol in cloud-free air
evaporation
collision scavenging
aqueous chemistry
activation, nucleation scavenging
precipitation formation
wet deposition
below-cloud scavenging

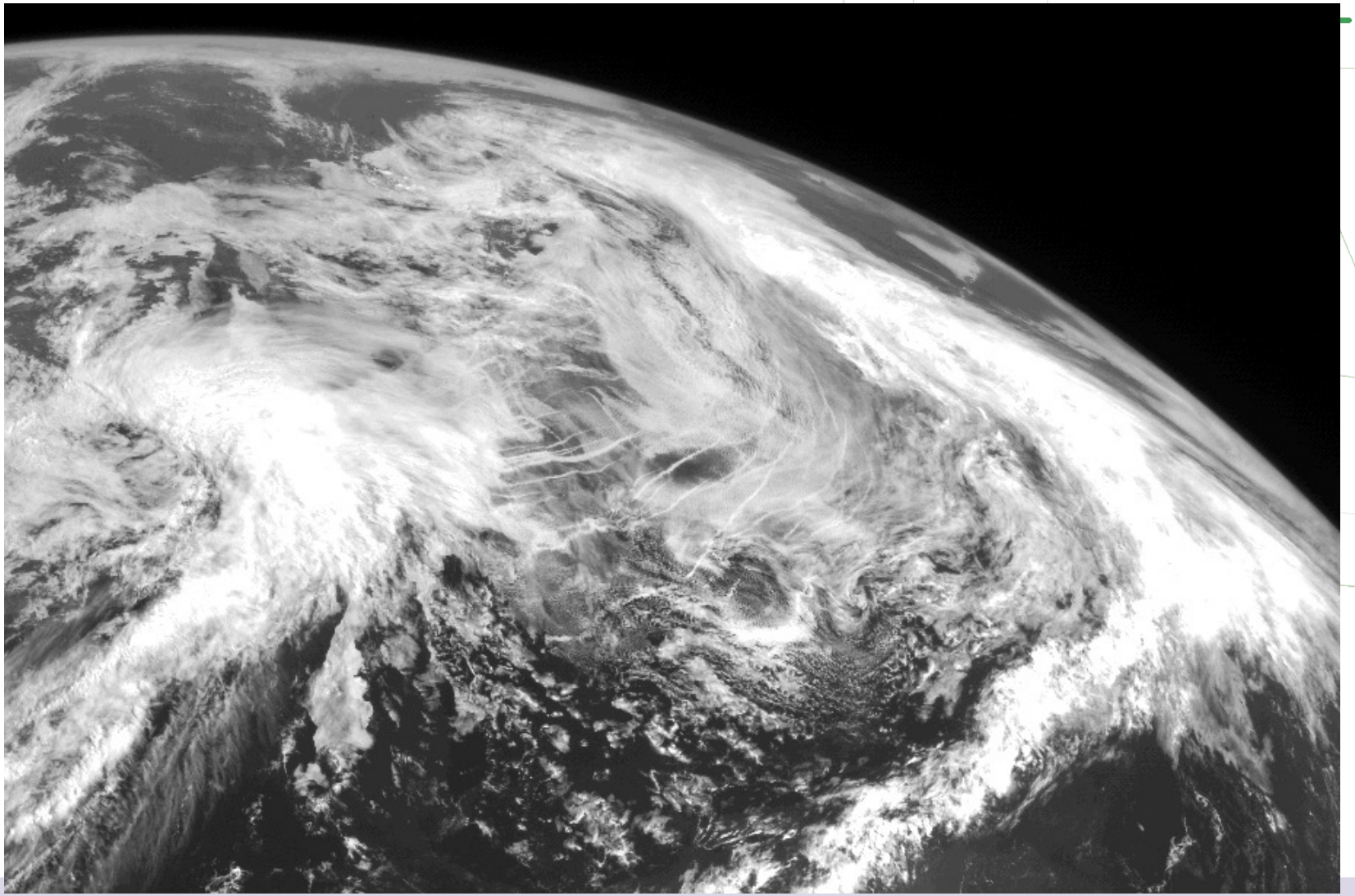

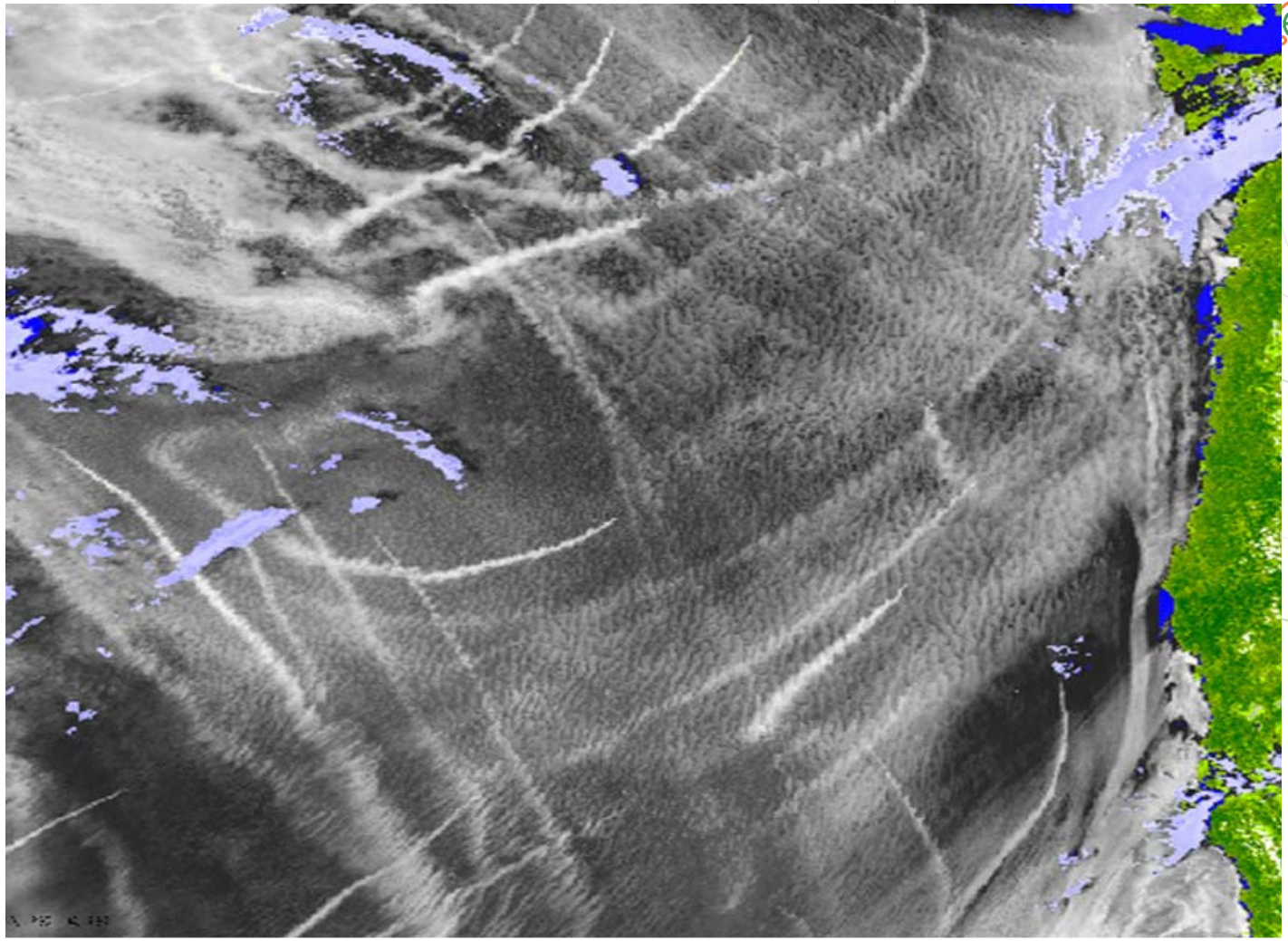

1. Homogeneous–homomolecular: self-nucleation of a single species. No foreign nuclei or surfaces involved.
2. Homogeneous–heteromolecular: self-nucleation of two or more species. No foreign nuclei or surfaces involved.
3. Heterogeneous–homomolecular: nucleation of a single species on a foreign substance.
4. Heterogeneous–heteromolecular: nucleation of two or more species on a foreign substance.

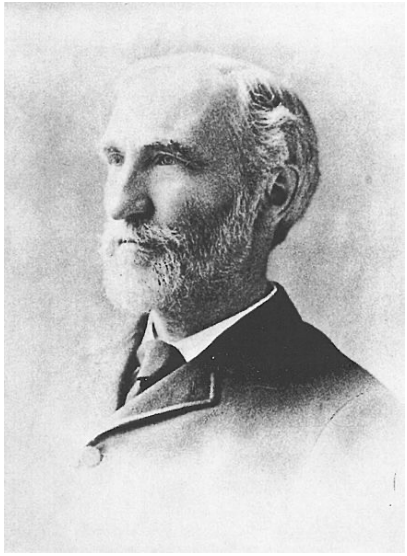

Josiah Willard Gibbs
(1839-1903)

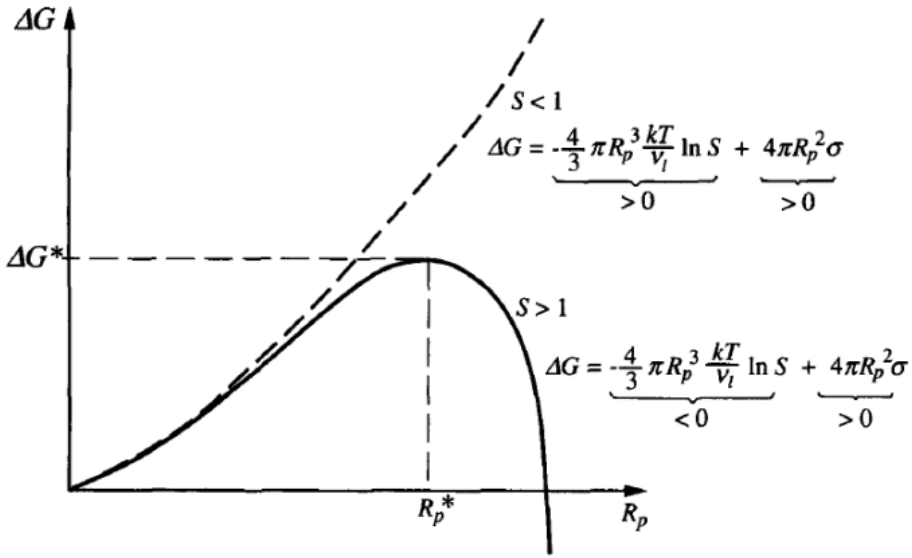

FIGURE 10.10 Gibbs free energy change for formation of a droplet of radius R_p from a vapor with saturation ratio S.

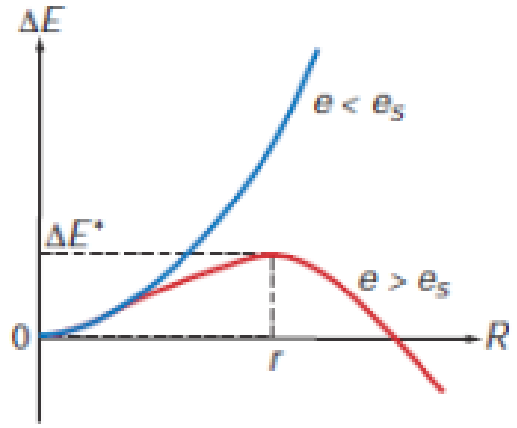

Fig. 6.1 Increase ΔE in the energy of a system due to the formation of a water droplet of radius R from water vapor with pressure e; e_s is the saturation vapor pressure with respect to a plane surface of water at the temperature of the system.

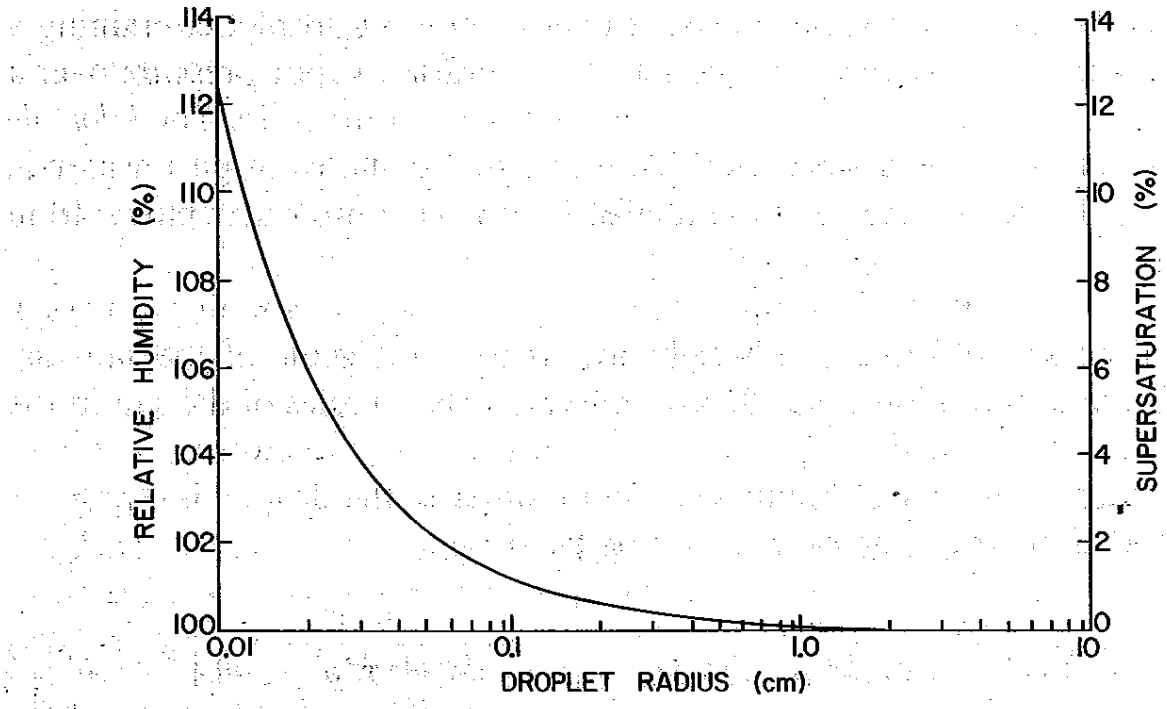

Fig. 4.11 The relative humidity and supersaturation (both with respect to a plane surface of liquid water) with which pure water droplets are in (unstable) equilibrium at 5°C.

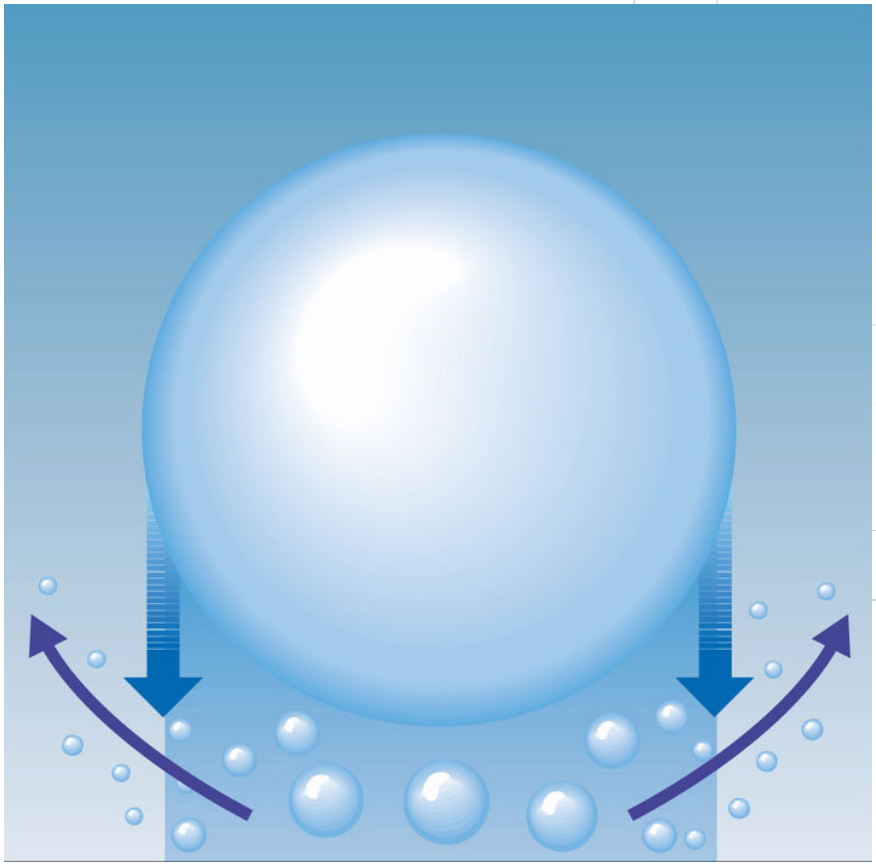

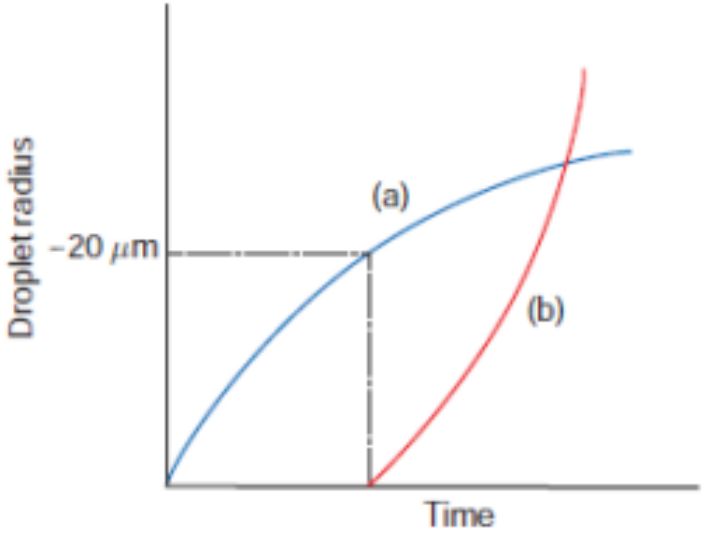

Fig. 6.15 Schematic curves of droplet growth (a) by condensation from the vapor phase (blue curve) and (b) by collection of droplets (red curve).

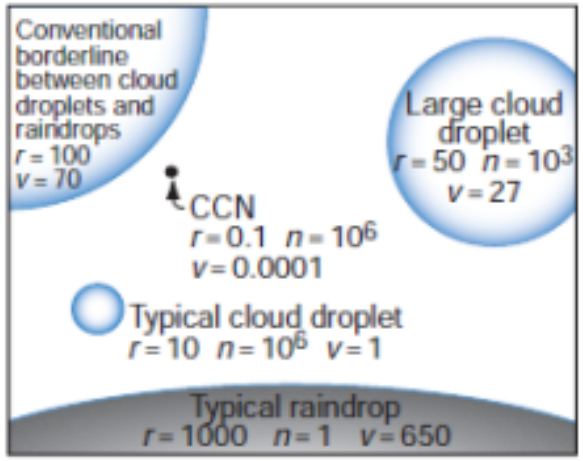

Fig. 6.18 Relative sizes of cloud droplets and raindrops; r is the radius in micrometers, n is the number per liter of air, and v is the terminal fall speed in centimeters per second. The circumferences of the circles are drawn approximately to scale, but the black dot representing a typical CCN is 25 times larger than it should be relative to the other circles. [Adapted from J. E. MacDonald, "The physics of cloud modification," *Adv. Geophys.* 5, 244 (1958). Copyright 1958, with permission from Elsevier.]

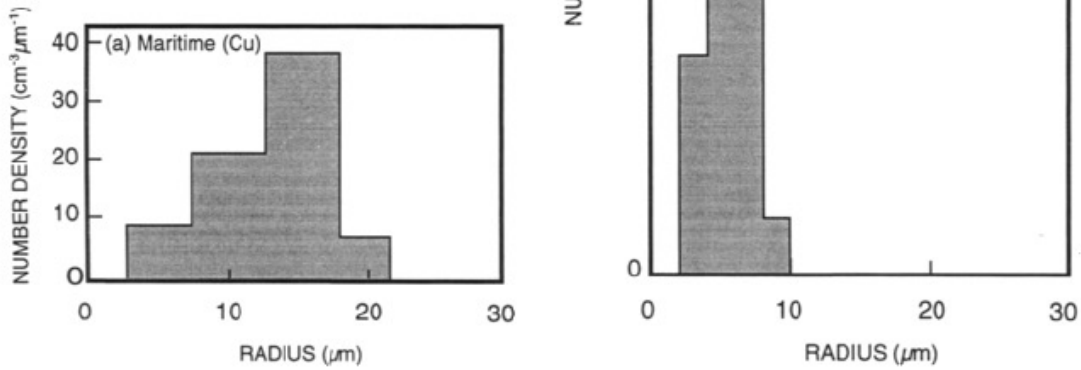

Figure 9.10 Droplet size spectra for cumulus cloud in (a) maritime environment and (b) continental environment. Note the compressed scale in (b). Area under each curve reflects the overall number density n, which is an order of magnitude greater in continental cumulus than in maritime cumulus. Source: Pruppacher (1981).

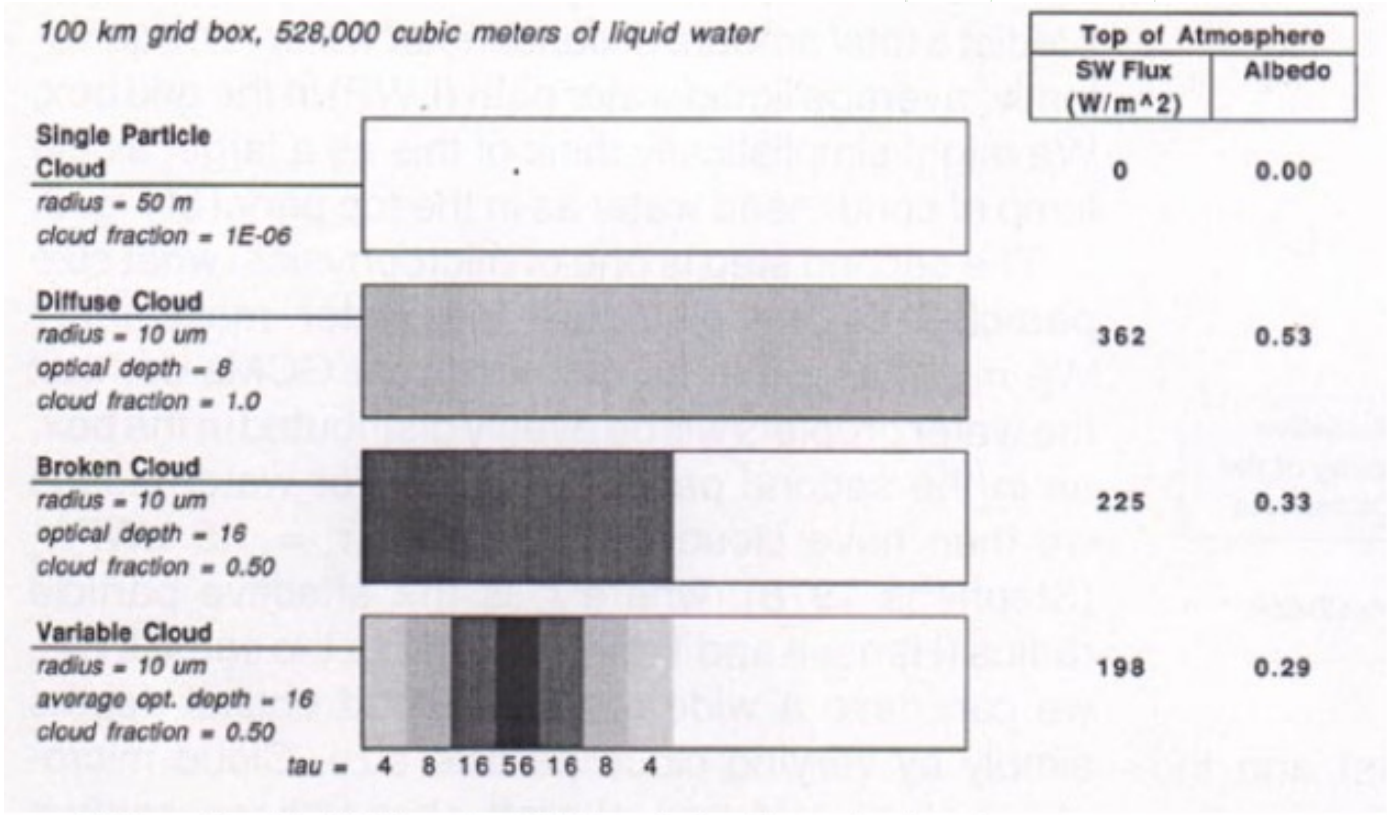

All Cases: Plane Parallel, Independent Pixel Approximation, Conservative Scattering, Surface Albedo = 0, g = 0.86, Solar Zenith = 60 degrees.

FIG. 9. Schematic diagram of varying distributions of cloud liquid water in a global climate model, and their impact on calculations of TOA SW reflected fluxes. All cases have equal total liquid water.

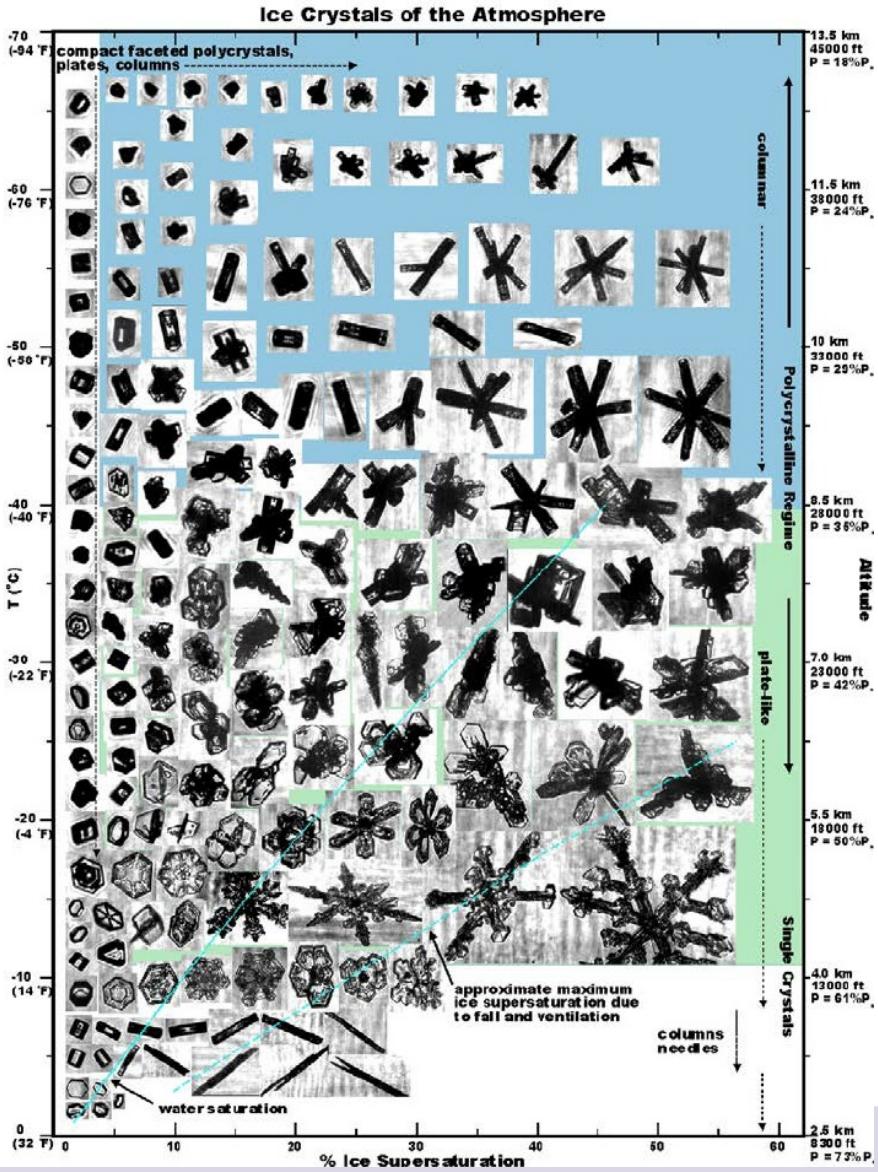

Ice crystal shape as a function of formation temperature and supersaturation with respect to ice. Right axis gives approximate height and pressure of crystal formation where P o is standard atmosphere pressure. Figure adapted from Bailey and Hallett (2009), courtesy of Dr. Bailey.

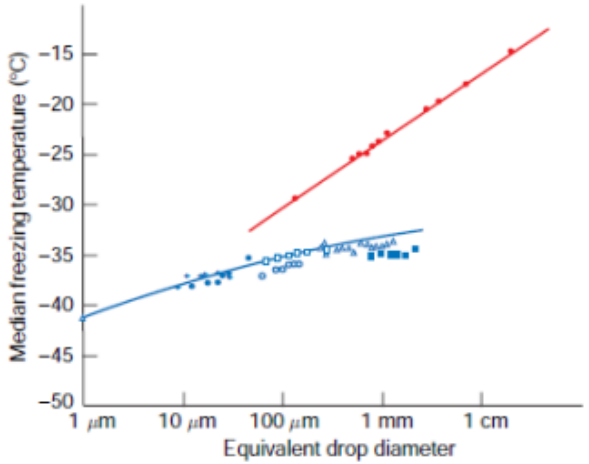

Fig. 6.29 Median freezing temperatures of water samples as a function of their equivalent drop diameter. The different symbols are results from different workers. The red symbols and red line represent heterogeneous freezing, and the blue symbols and line represent homogeneous freezing. [Adapted from B. J. Mason, *The Physics of Clouds*, Oxford Univ. Press, Oxford, 1971, p. 160. By permission of Oxford University Press.]

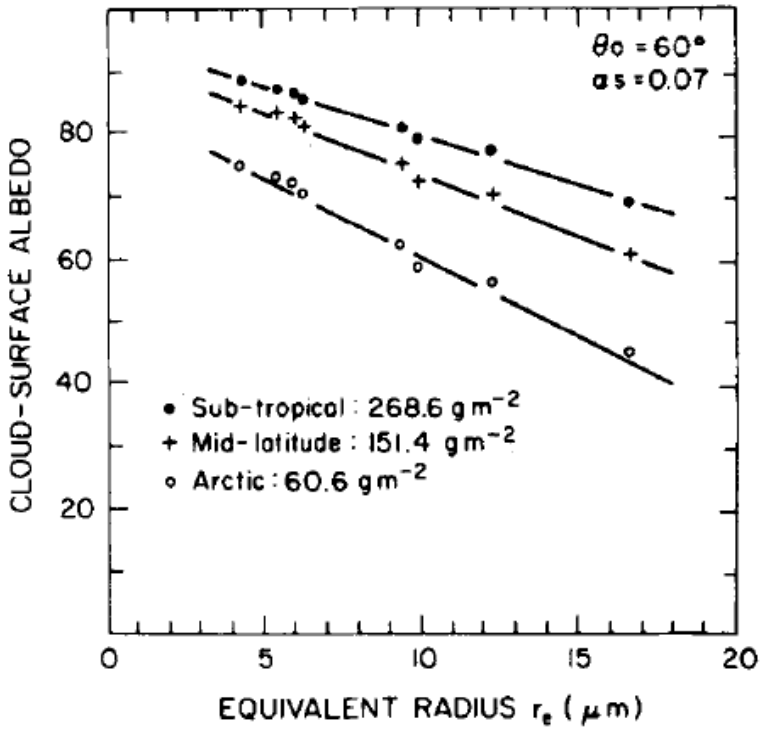

Fig. 3.14 The dependence of planetary albedo on the size of cloud droplets. [From Slingo and Schrecker (1982). Reprinted with permission from the Royal Meteorological Society.]

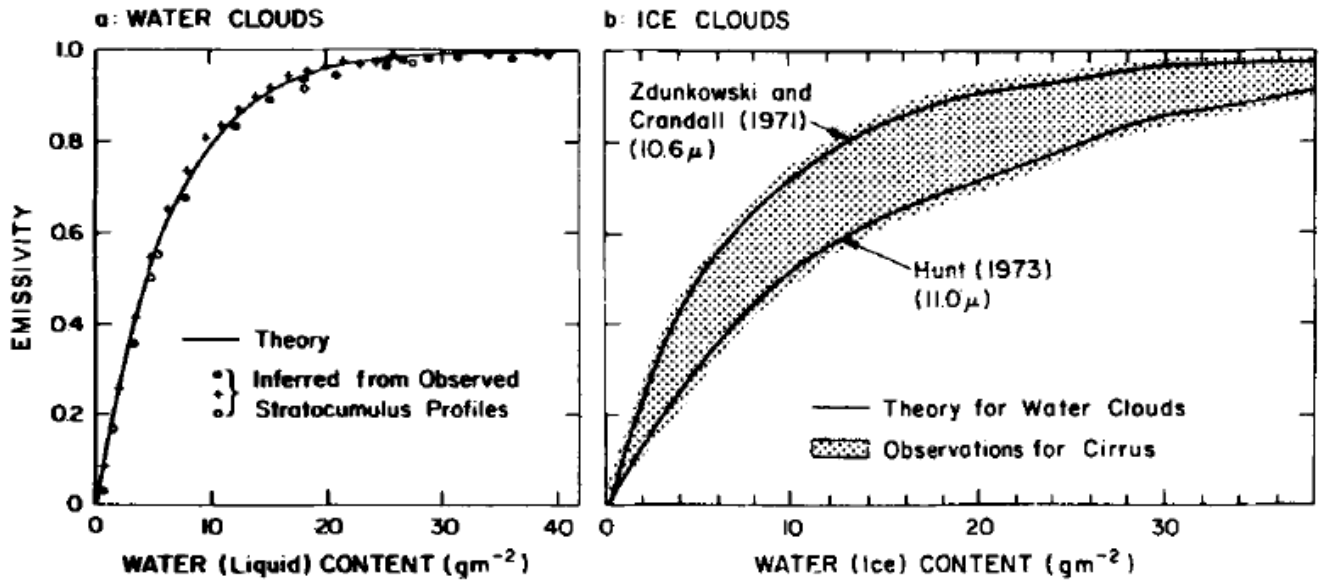

Fig. 3.15 The dependence of the longwave emissivity on (a) liquid water content [from Slingo *et al.* (1982); reprinted with permission from the Royal Meteorological Society] and (b) ice content [from Griffith *et al.* (1980); reprinted with permission from the American Meteorological Society].

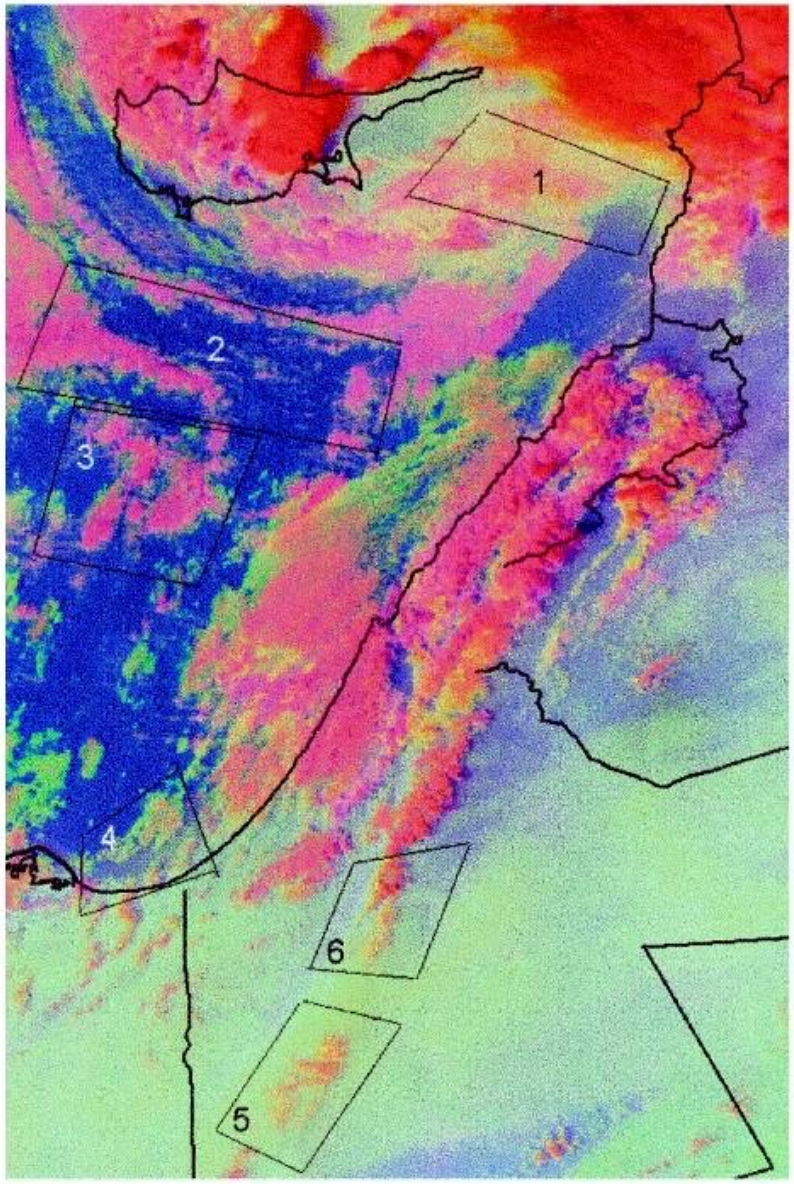

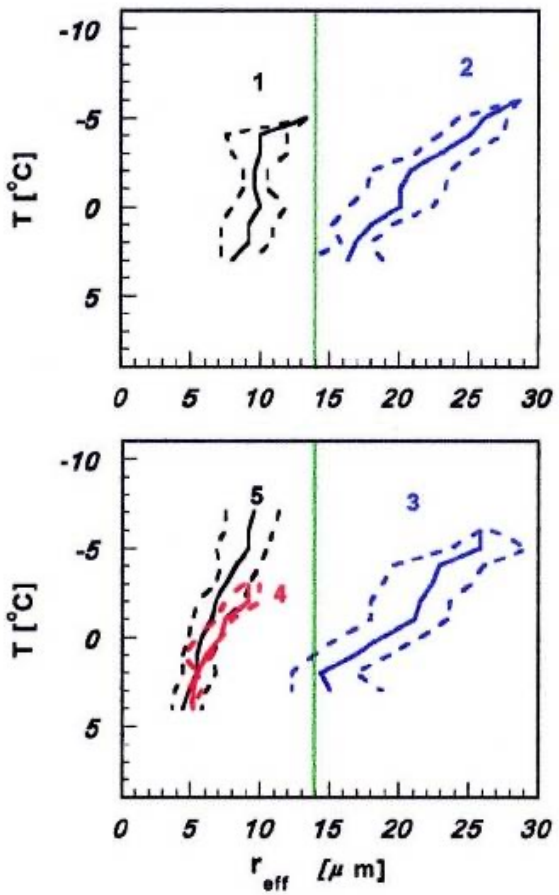

Rosenfeld et al., 2001

IPCC, 2021

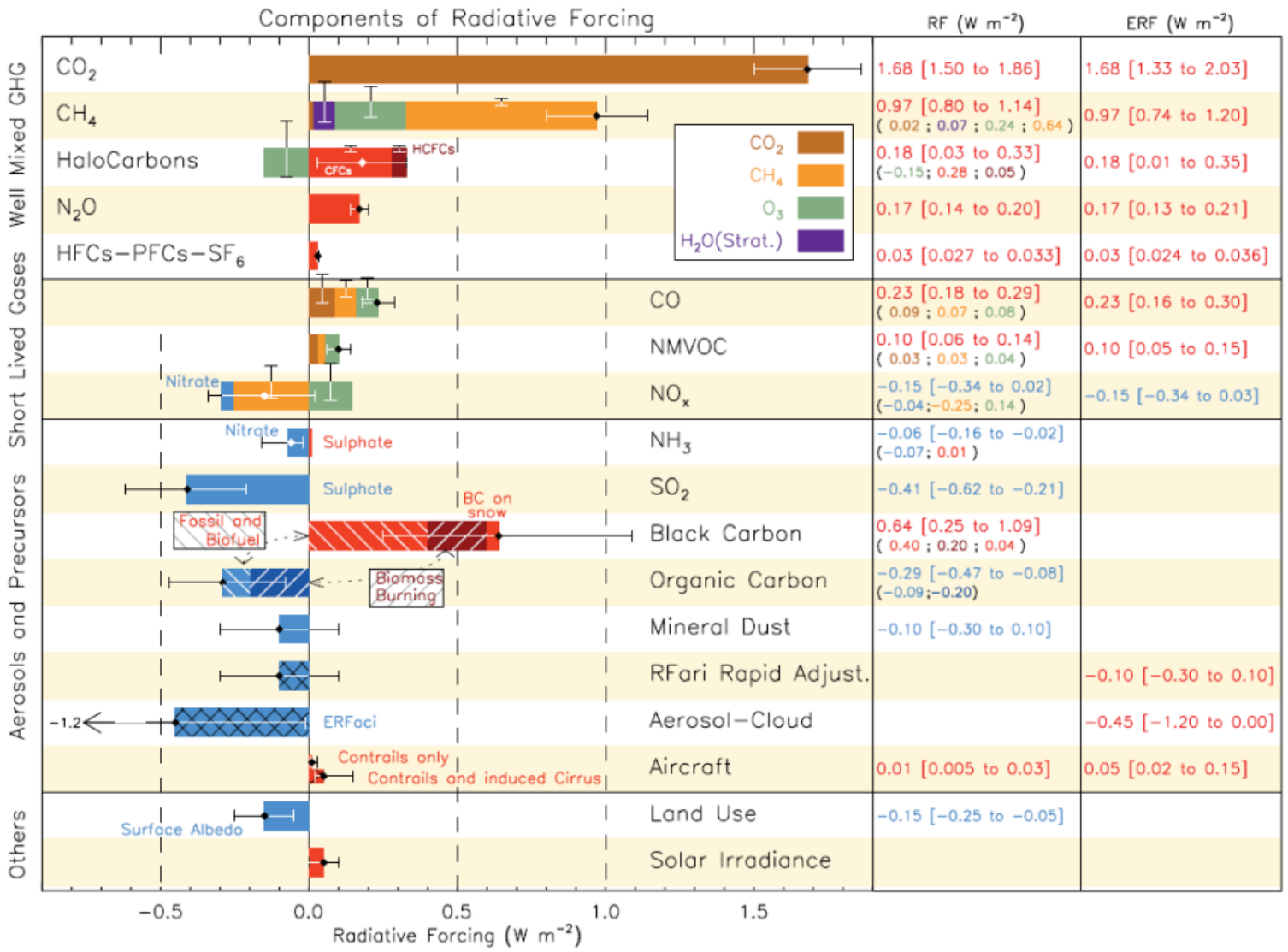
Components of Radiative Forcing
RF (W m⁻²)
ERF (W m⁻²)
Well Mixed GHG
Short Lived Gases
Aerosols and Precursors
Others
CO2
CH4
HaloCarbons
HCFCs
CFCs
N2O
HFCs–PFCs–SF6
CO2
CH4
O3
H2O(Strat.)
CO
NMVOC
NOx
Nitrate
NH3
Nitrate
Sulphate
SO2
Sulphate
BC on snow
Fossil and Biofuel
Black Carbon
Organic Carbon
Biomass Burning
Mineral Dust
RFari Rapid Adjust.
-1.2
ERFaci
Aerosol–Cloud
Contrails only
Contrails and induced Cirrus
Aircraft
Land Use
Surface Albedo
Solar Irradiance
1.68 [1.50 to 1.86]
1.68 [1.33 to 2.03]
0.97 [0.80 to 1.14]
(0.02 ; 0.07 ; 0.24 ; 0.64)
0.97 [0.74 to 1.20]
0.18 [0.03 to 0.33]
(−0.15; 0.28 ; 0.05)
0.18 [0.01 to 0.35]
0.17 [0.14 to 0.20]
0.17 [0.13 to 0.21]
0.03 [0.027 to 0.033]
0.03 [0.024 to 0.036]
0.23 [0.18 to 0.29]
(0.09 ; 0.07 ; 0.08)
0.23 [0.16 to 0.30]
0.10 [0.06 to 0.14]
(0.03 ; 0.03 ; 0.04)
0.10 [0.05 to 0.15]
−0.15 [−0.34 to 0.02]
(−0.04;−0.25; 0.14)
−0.15 [−0.34 to 0.03]
−0.06 [−0.16 to −0.02]
(−0.07; 0.01)
−0.41 [−0.62 to −0.21]
0.64 [0.25 to 1.09]
(0.40 ; 0.20 ; 0.04)
−0.29 [−0.47 to −0.08]
(−0.09;−0.20)
−0.10 [−0.30 to 0.10]
−0.10 [−0.30 to 0.10]
−0.45 [−1.20 to 0.00]
0.01 [0.005 to 0.03]
0.05 [0.02 to 0.15]
−0.15 [−0.25 to −0.05]
−0.5
0.0
0.5
1.0
1.5
Radiative Forcing (W m⁻²)

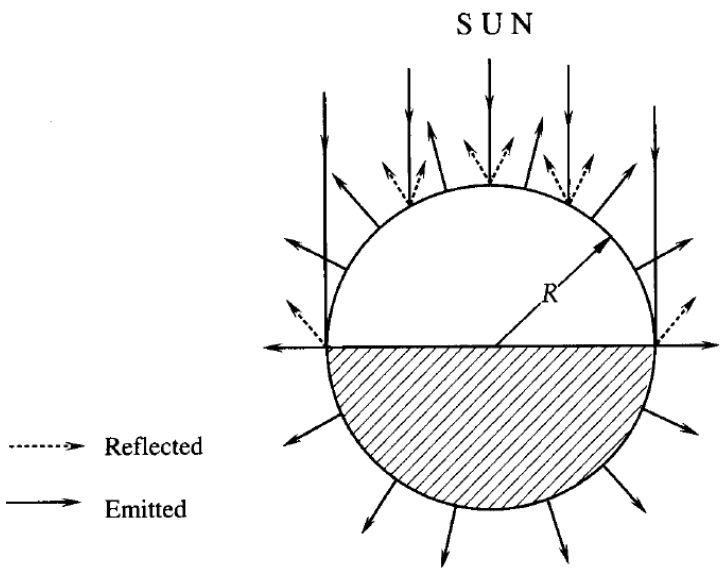

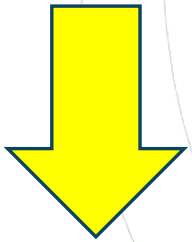

340 W/m²

100 W/m²

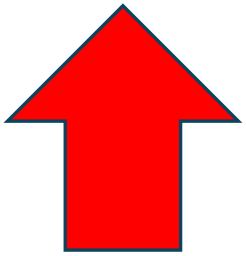

240 W/m²

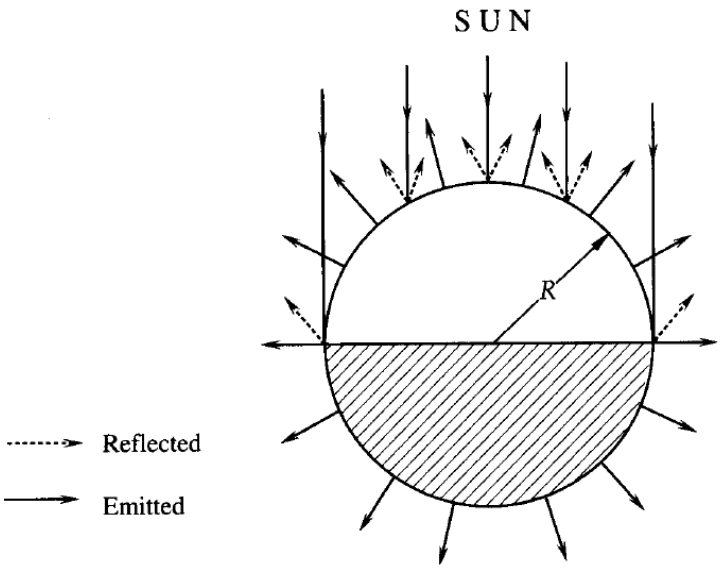

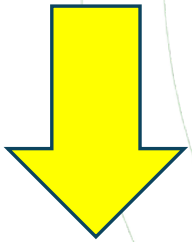

340 W/m²

50 W/m²

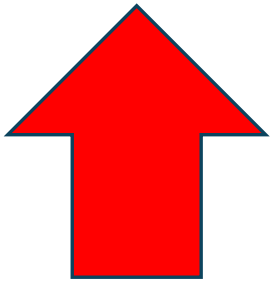

270 W/m²

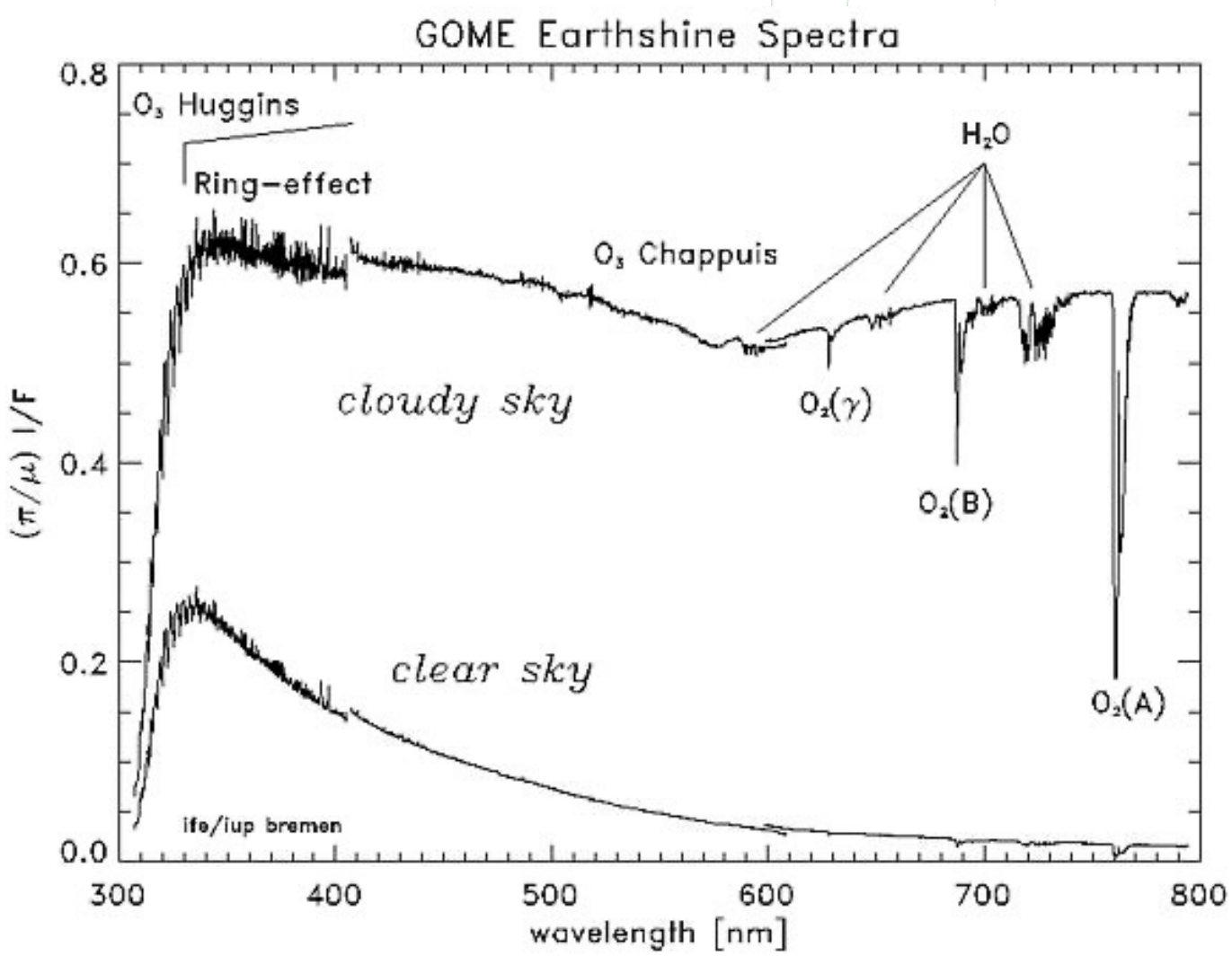
GOME Earthshine Spectra
O₃ Huggins
Ring-effect
O₃ Chappuis
H₂O
cloudy sky
clear sky
O₂(γ)
O₂(B)
O₂(A)
ife/iup bremen
(π/μ) I/F
wavelength [nm]
0.0
0.2
0.4
0.6
0.8
300
400
500
600
700
800

Examples of AIRS Spectra

20-July-2002 Ascending LW_Window

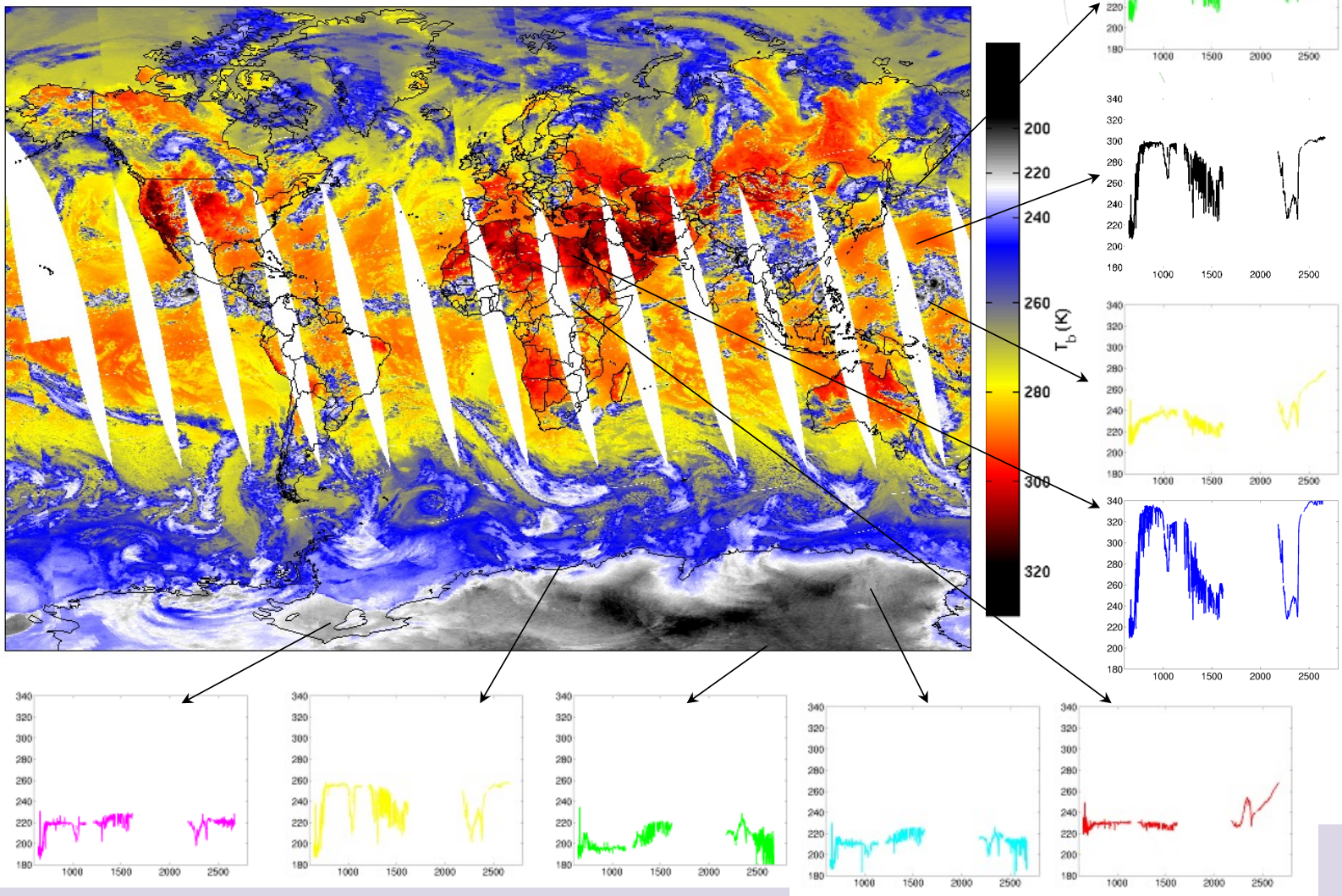

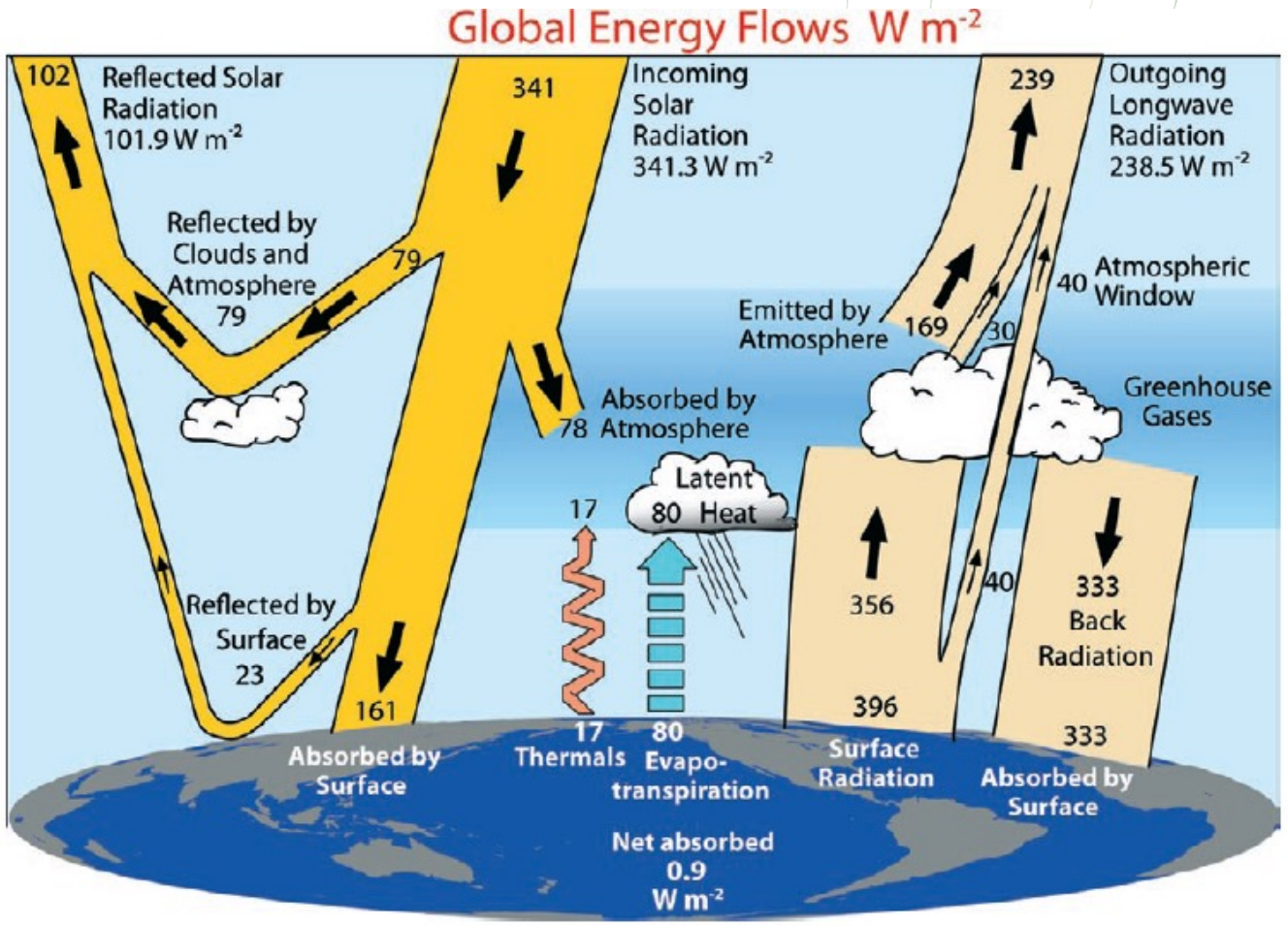

FIG. 1. The global annual mean Earth's energy budget for the Mar 2000 to May 2004 period (W m^{-2}). The broad arrows indicate the schematic flow of energy in proportion to their importance.

Trenberth et al., 2009

Absorption

Scattering

Emission

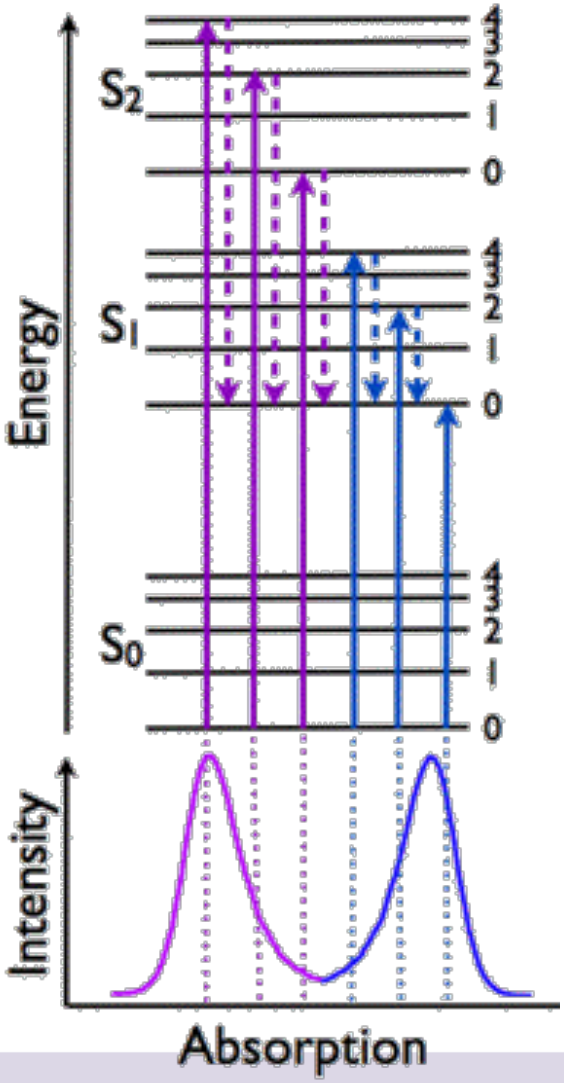

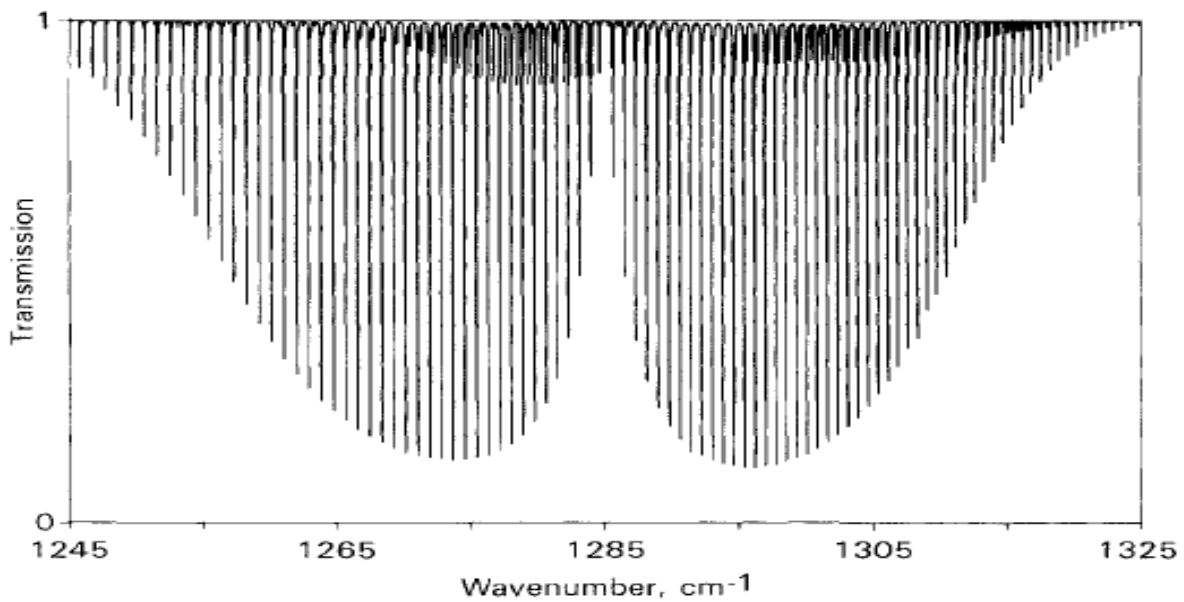

FIG. 3.3. Synthetic spectrum of N_2O near 7.78 μm. Spectral range: 1245–1325 cm^{-1}. Altitude of observation: 15 km. Zenith angle of observation: 30°. Terrestrial concentration ×1.

$$E_{\text{total}} = E_{\text{translational}} + E_{\text{rotational}} + E_{\text{vibrational}} + E_{\text{electronic}}$$

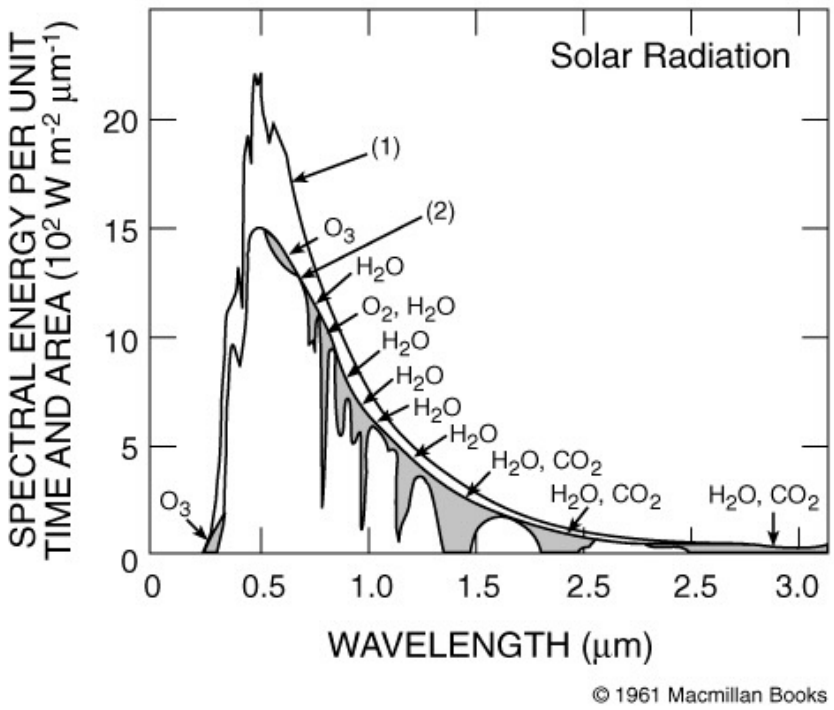

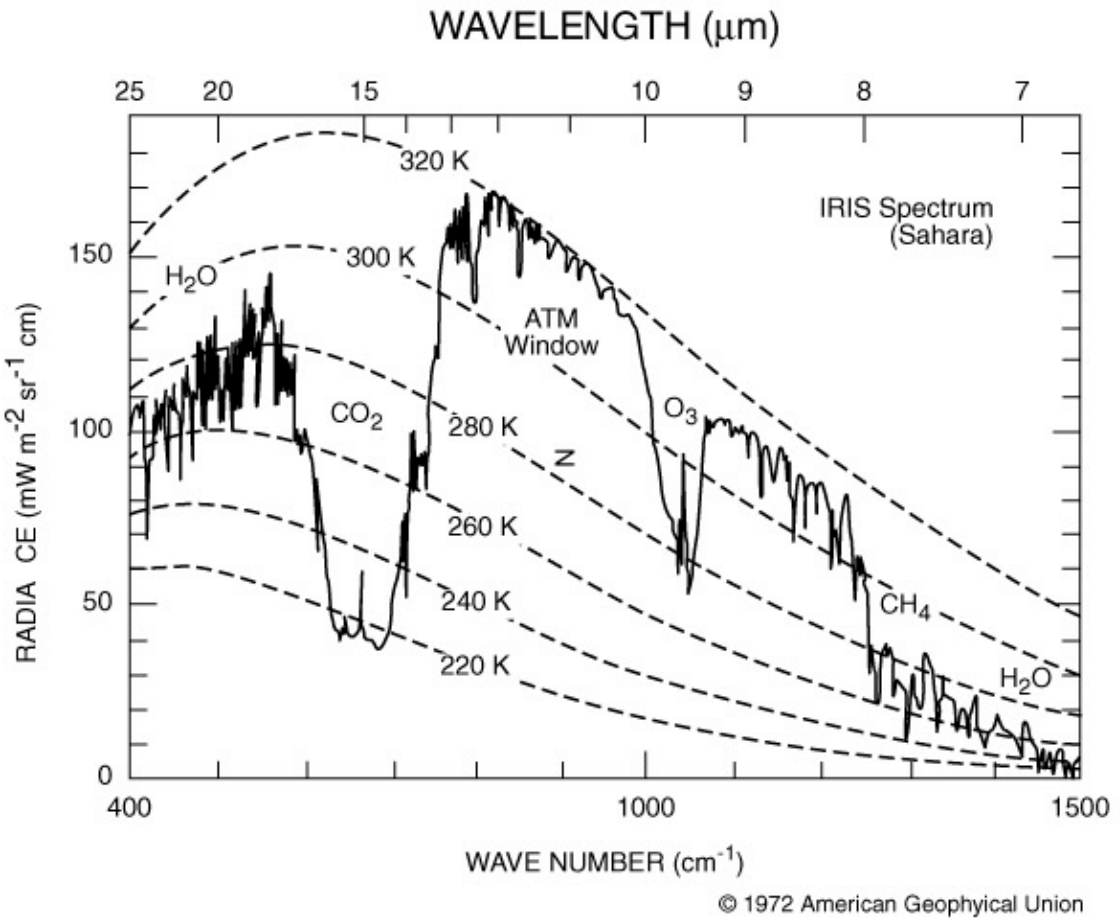

Aerosol/clouds absorption?

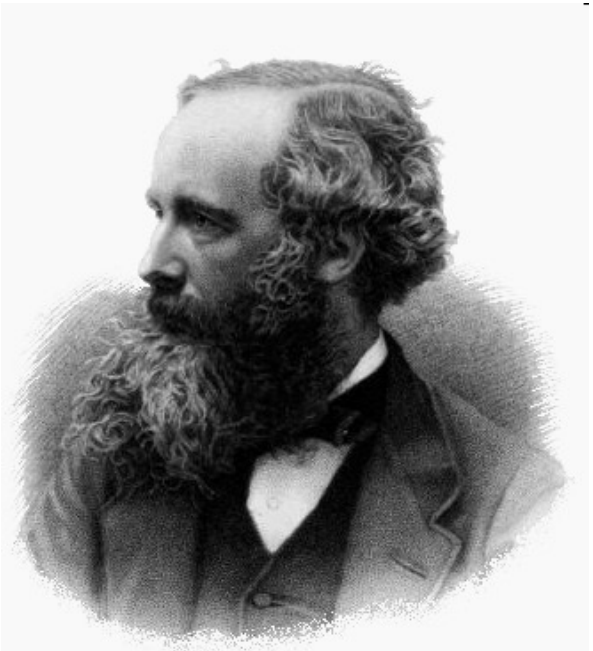

James Clerk Maxwell
(1831–1879)

$$\begin{cases} \nabla \cdot \mathbf{E} = \dfrac{\rho}{\epsilon_0} \\ \nabla \times \mathbf{E} = -\dfrac{\partial \mathbf{B}}{\partial t} \\ \nabla \cdot \mathbf{B} = 0 \\ \nabla \times \mathbf{B} = \mu_0 \mathbf{J} + \epsilon_0 \mu_0 \dfrac{\partial \mathbf{E}}{\partial t} \end{cases}$$

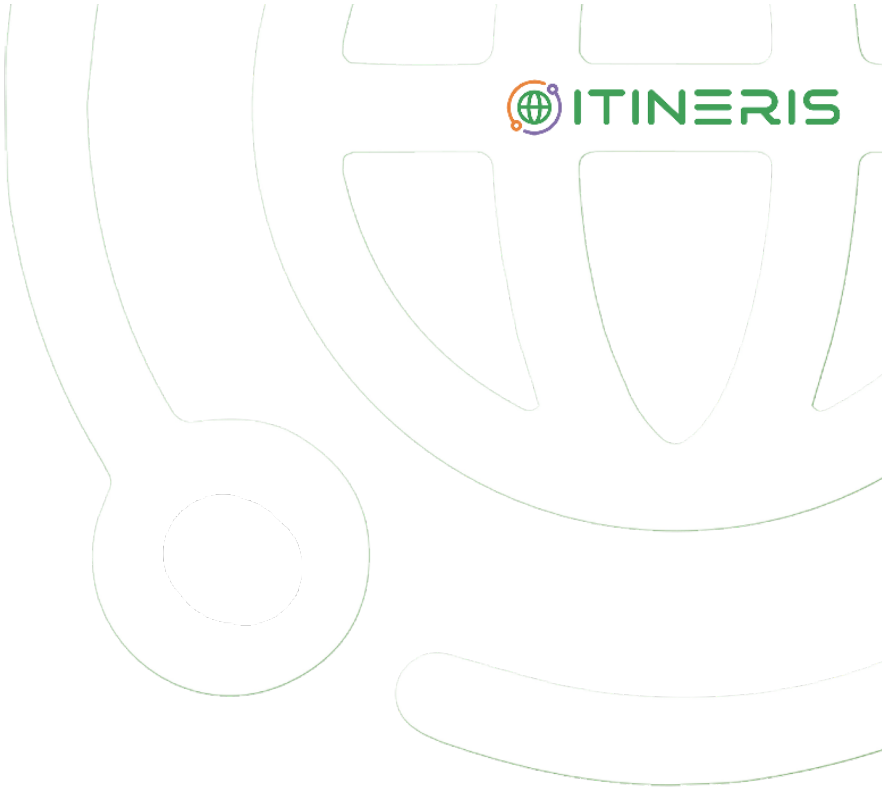
ITINERIS

Absorption
Scattering
Emission

John William Strutt
3rd Baron Rayleigh
(1842–1919)

$$\sigma = \frac{24\pi^3(n_s^2 - 1)^2}{\lambda^4 N_s^2 (n_s^2 + 2)^2}\left(\frac{6 + 3\rho}{6 - 7\rho}\right),$$

$$\tau_R(\lambda) = \frac{p}{p_0} 0.008\ 77\lambda^{-4.05}$$

Dutton et al., 1994

$$\tau_R(\lambda) = 0.008\ 569\lambda^{-4}(1 + 0.0113\lambda^{-2} + 0.000\ 13\lambda^{-4}),$$

Hanson and Travis, 1974

1871

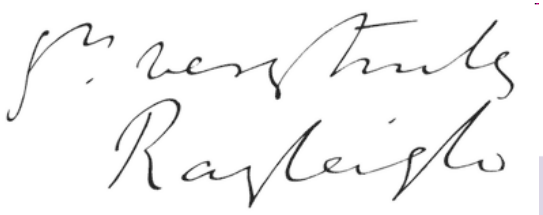

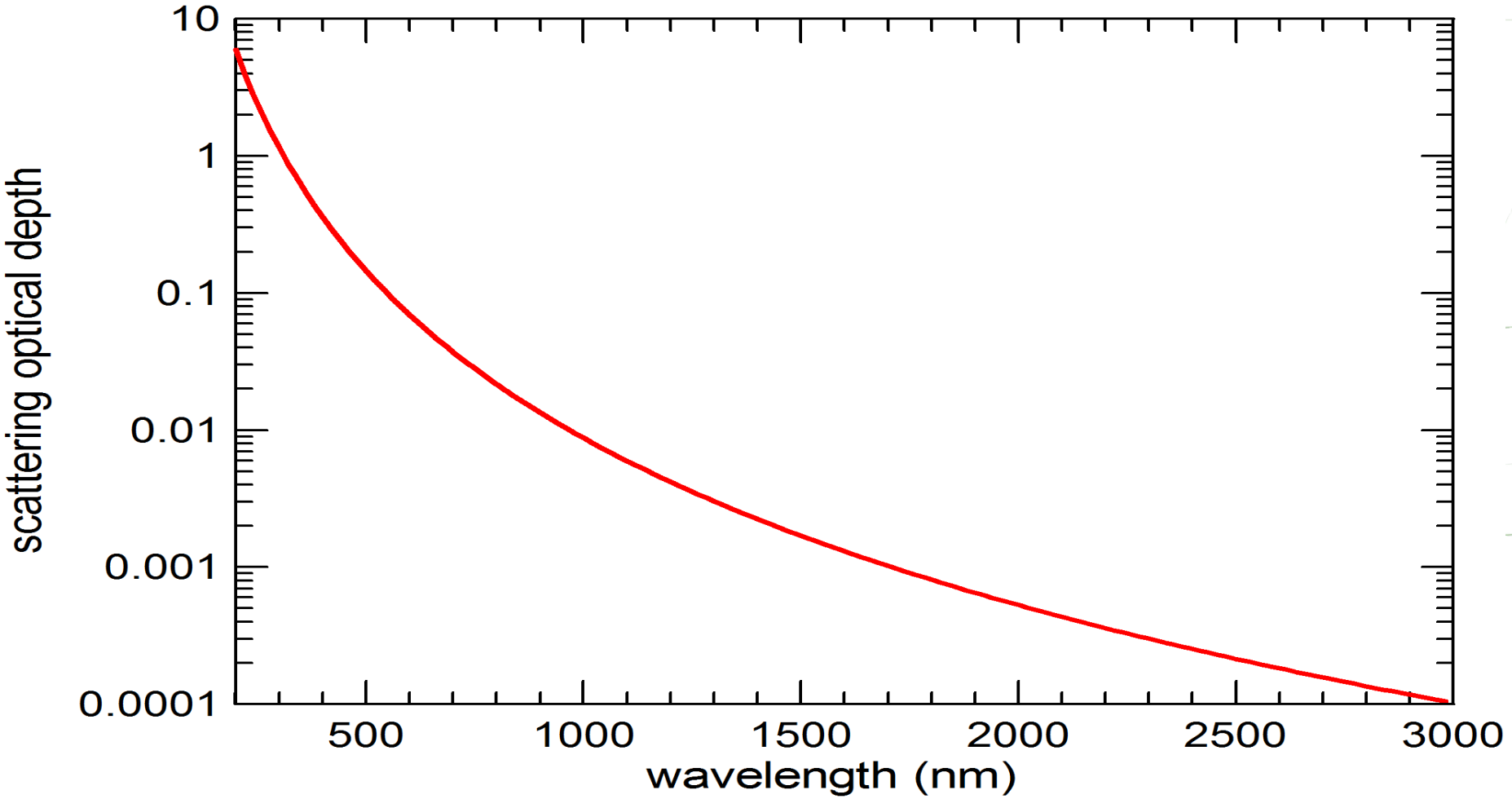
scattering optical depth
10
1
0.1
0.01
0.001
0.0001
500
1000
1500
2000
2500
3000
wavelength (nm)

TABLE 3. Scattering cross section (per molecule) and Rayleigh optical depth (τ_R) for dry air containing 360 ppm CO_2. Rayleigh optical depths are given for a location at sea level, 1013.25 mb, 45° latitude, and at MLO at altitude 3400 m, pressure 680 mb, and latitude 19.533°.

WV (μm)	σ (cm^2)	τ_R (sea level, 45°N)	τ_R (MLO, 680 mb)	King factor
0.250	1.2610E−25	2.7137E+00	1.8264E+00	1.06308
0.255	1.1537E−25	2.4828E+00	1.6710E+00	1.06215
0.260	1.0579E−25	2.2766E+00	1.5322E+00	1.06130
0.265	9.7206E−26	2.0919E+00	1.4079E+00	1.06052
0.270	8.9496E−26	1.9260E+00	1.2962E+00	1.05979
0.275	8.2552E−26	1.7766E+00	1.1956E+00	1.05912
0.280	7.6282E−26	1.6416E+00	1.1048E+00	1.05850
0.285	7.0608E−26	1.5195E+00	1.0227E+00	1.05793
0.290	6.5462E−26	1.4088E+00	9.4813E−01	1.05739
0.295	6.0785E−26	1.3081E+00	8.8038E−01	1.05689
0.300	5.6525E−26	1.2164E+00	8.1868E−01	1.05643
0.305	5.2638E−26	1.1328E+00	7.6238E−01	1.05599
0.310	4.9084E−26	1.0563E+00	7.1092E−01	1.05559
0.315	4.5830E−26	9.8629E−01	6.6379E−01	1.05521
0.320	4.2846E−26	9.2206E−01	6.2056E−01	1.05485
0.325	4.0103E−26	8.6304E−01	5.8084E−01	1.05452
0.330	3.7580E−26	8.0873E−01	5.4429E−01	1.05421
0.335	3.5254E−26	7.5868E−01	5.1060E−01	1.05391
0.340	3.3108E−26	7.1249E−01	4.7952E−01	1.05363
0.345	3.1124E−26	6.6981E−01	4.5079E−01	1.05337
0.350	2.9289E−26	6.3031E−01	4.2421E−01	1.05312
0.500	6.6614E−27	1.4336E−01	9.6480E−02	1.04935
0.505	6.3951E−27	1.3763E−01	9.2624E−02	1.04929
0.510	6.1421E−27	1.3218E−01	8.8959E−02	1.04923
0.515	5.9015E−27	1.2700E−01	8.5475E−02	1.04917
0.520	5.6727E−27	1.2208E−01	8.2161E−02	1.04911
0.525	5.4549E−27	1.1739E−01	7.9006E−02	1.04906
0.530	5.2475E−27	1.1293E−01	7.6002E−02	1.04901
0.535	5.0499E−27	1.0868E−01	7.3140E−02	1.04896
0.540	4.8615E−27	1.0462E−01	7.0412E−02	1.04891
0.545	4.6819E−27	1.0076E−01	6.7811E−02	1.04886
0.550	4.5105E−27	9.7069E−02	6.5329E−02	1.04882

WV (μm)	σ (cm^2)	τ_R (sea level, 45°N)	τ_R (MLO, 680 mb)	King factor
0.885	6.5638E−28	1.4126E−02	9.5067E−03	1.04745
0.900	6.1339E−28	1.3200E−02	8.8841E−03	1.04742
0.905	5.9985E−28	1.2909E−02	8.6880E−03	1.04741
0.910	5.8668E−28	1.2626E−02	8.4972E−03	1.04740
0.915	5.7387E−28	1.2350E−02	8.3117E−03	1.04740
0.920	5.6141E−28	1.2082E−02	8.1312E−03	1.04739
0.925	5.4929E−28	1.1821E−02	7.9556E−03	1.04738
0.930	5.3749E−28	1.1567E−02	7.7848E−03	1.04737
0.935	5.2601E−28	1.1320E−02	7.6184E−03	1.04737
0.940	5.1483E−28	1.1079E−02	7.4566E−03	1.04736
0.945	5.0395E−28	1.0845E−02	7.2989E−03	1.04735
0.950	4.9335E−28	1.0617E−02	7.1455E−03	1.04734
0.955	4.8303E−28	1.0395E−02	6.9960E−03	1.04734
0.960	4.7298E−28	1.0179E−02	6.8505E−03	1.04733
0.965	4.6319E−28	9.9682E−03	6.7087E−03	1.04732
0.970	4.5366E−28	9.7629E−03	6.5706E−03	1.04732
0.975	4.4437E−28	9.5630E−03	6.4360E−03	1.04731
0.980	4.3531E−28	9.3681E−03	6.3049E−03	1.04730
0.985	4.2649E−28	9.1782E−03	6.1770E−03	1.04730
0.990	4.1788E−28	8.9930E−03	6.0524E−03	1.04729
0.995	4.0950E−28	8.8125E−03	5.9310E−03	1.04728
1.000	4.0132E−28	8.6366E−03	5.8125E−03	1.04728

Bodhaine et al., 1999

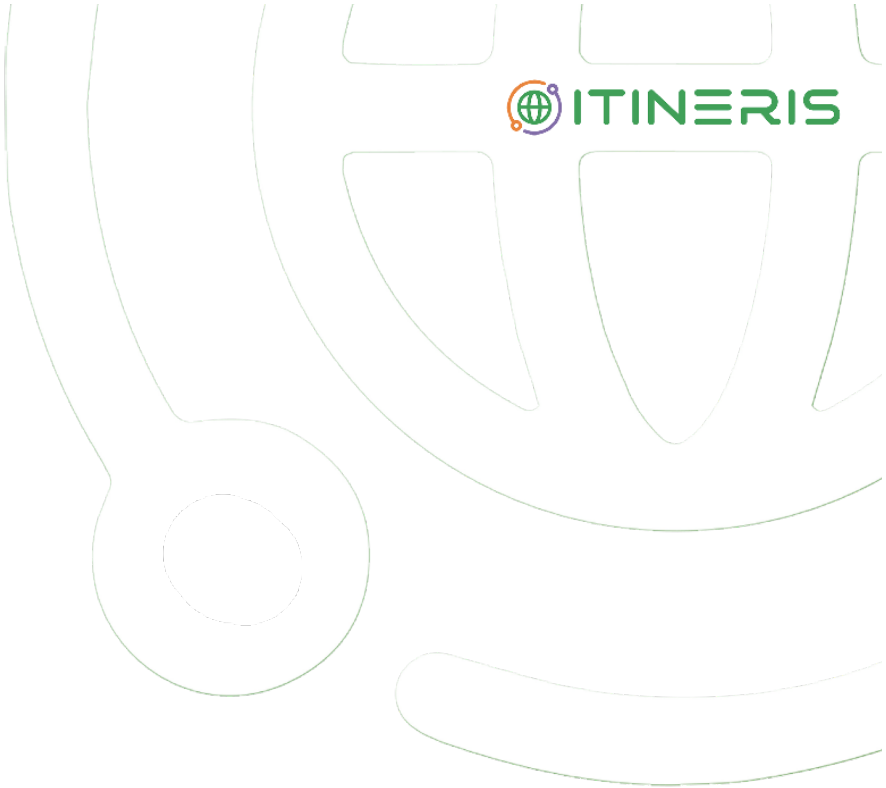
ITINERIS

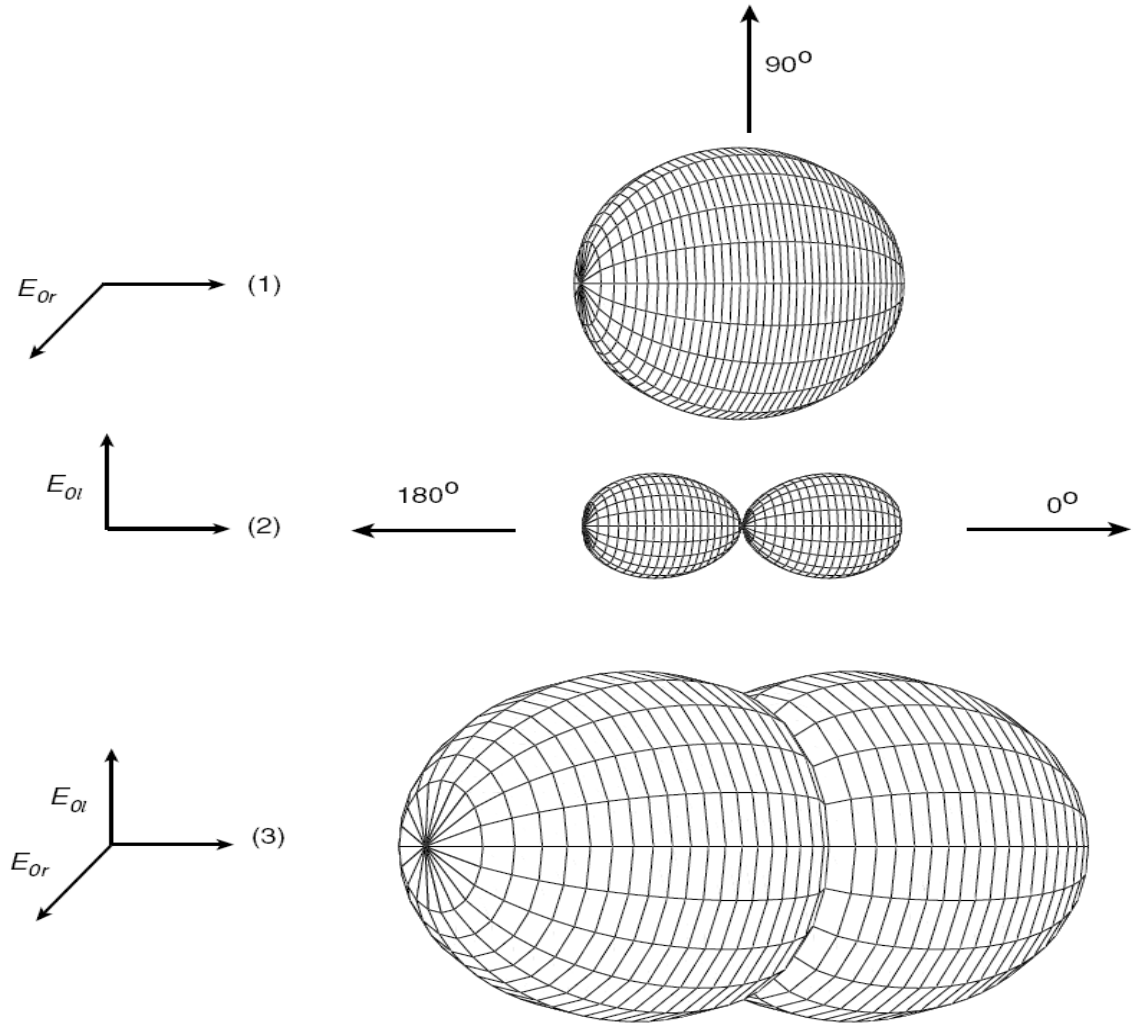

Figure 3.11 Polar diagram of the scattered intensity for Rayleigh molecules: (1) polarized incident light with the electric vector perpendicular to the scattering plane, (2) polarized incident light with the electric vector on the scattering plane, and (3) unpolarized incident light.

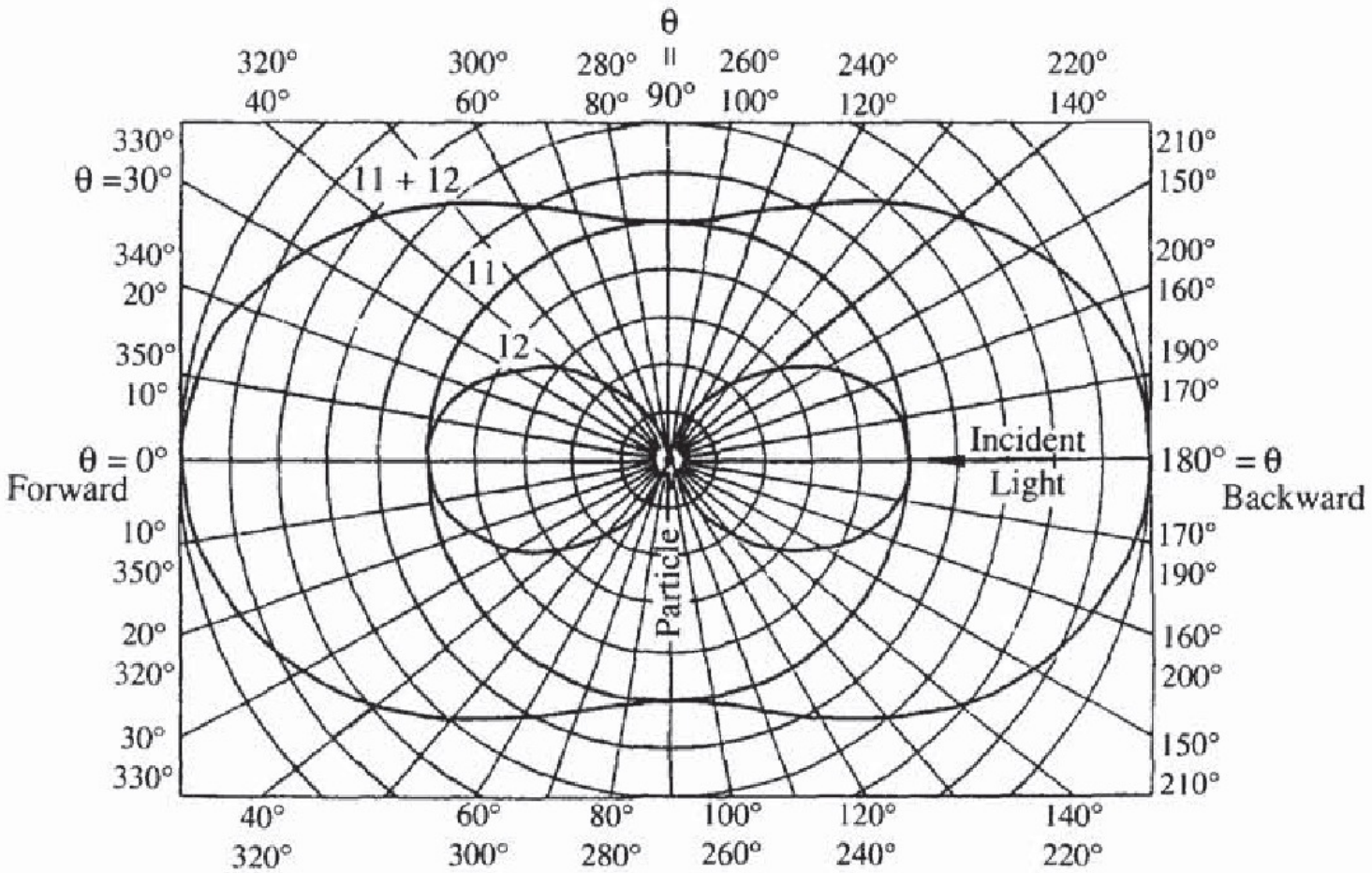

FIGURE 15.2 Pattern of light scattering (scattering phase function) by a particle in the Rayleigh regime. The scattered light intensity pattern is symmetric in the forward and backward directions, totally polarized at 90°, and independent of particle shape. Incident beam enters from the right. 11 indicates the circular component independent of θ; 12 is the θ-dependent term.

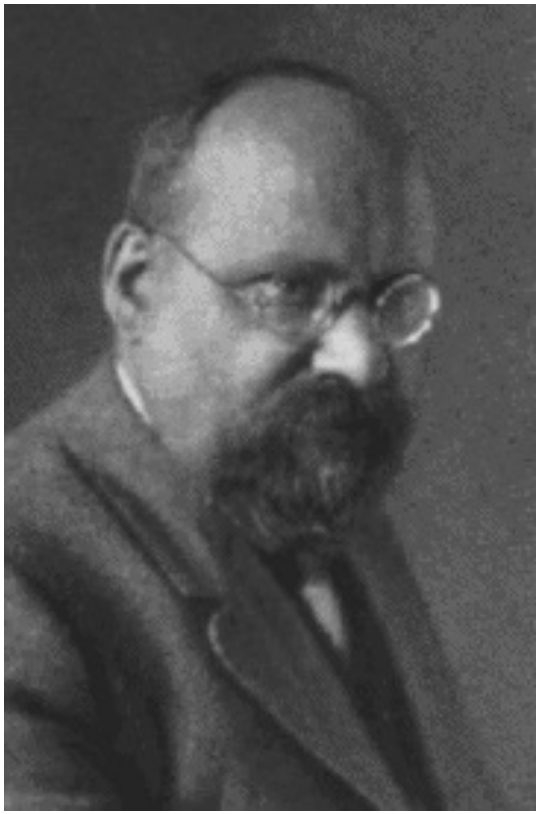

Gustav Adolf Feodor Wilhelm Ludwig Mie
(1869 -1957)

1908. № 3.

ANNALEN DER PHYSIK.

VIERTE FOLGE. BAND 25.

1. ***Beiträge zur Optik trüber Medien, speziell kolloidaler Metallösungen;***
von Gustav Mie.

1. Die mannigfachen Färbungen der Metalle im kolloidalen Zustand haben im Laufe der Zeiten recht verschiedenartige Deutungen erfahren. Früher neigte man sehr zu der Meinung, daß die betreffenden Metalle (besonders das Silber) in mehreren verschieden gefärbten Modifikationen aufträten. Später ist die Meinung aufgekommen, daß die Farben auf optischer Resonanz beruhten. Diese Meinung ist besonders eingehend von F. Ehrenhaft[1]) begründet worden. Endlich hat neuerdings J. C. Maxwell-Garnett[2]) nachgewiesen, daß sich die Farben von kolloidalen Metallen, wenn die suspendierten Partikelchen des Metalles sehr klein sind, aus der Theorie, die L. Lorenz[3]) für optisch inhomogene Medien entwickelt hat, einwandsfrei erklären lassen. Die Theorie ergibt für eine feine Metallsuspension, in denen die Dimensionen der Teilchen im Vergleich zur Wellenlänge und außerdem zu ihren gegenseitigen Entfernungen sehr klein sind, eine ganz bestimmte Absorptionskurve, die sich aus den optischen Konstanten des Metalles vorher berechnen läßt und demnach, obwohl sie durchaus verschieden von der Absorptionskurve des soliden Metalles verläuft, doch gar nichts mit Resonanz in dem Sinne, in dem dieses Wort von Ehrenhaft, Wood u. a. gebraucht wird, zu tun hat. So konnte Maxwell-Garnett unter anderem die rote Farbe vieler Goldlösungen, die Ehrenhaft als Resonanz-

1) F. Ehrenhaft, Wiener Sitzungsber. IIa. **112.** p. 181. 1903; **114.** p. 1115. 1905.

2) J. C. Maxwell-Garnett, Phil. Trans. **203.** p. 385. 1904; **205.** p. 237. 1906. Für den Brechungsexponenten von Gelatine-Silberemulsionen wies auch F. Kirchner in seiner Leipziger Dissertation die Gültigkeit der Lorenzschen Formel nach (Ann. d. Phys. **13.** p. 239. 1904).

3) L. Lorenz, Wied. Ann. **11.** p. 70. 1880.

Ludvig Valentin Lorenz (1829-1891)

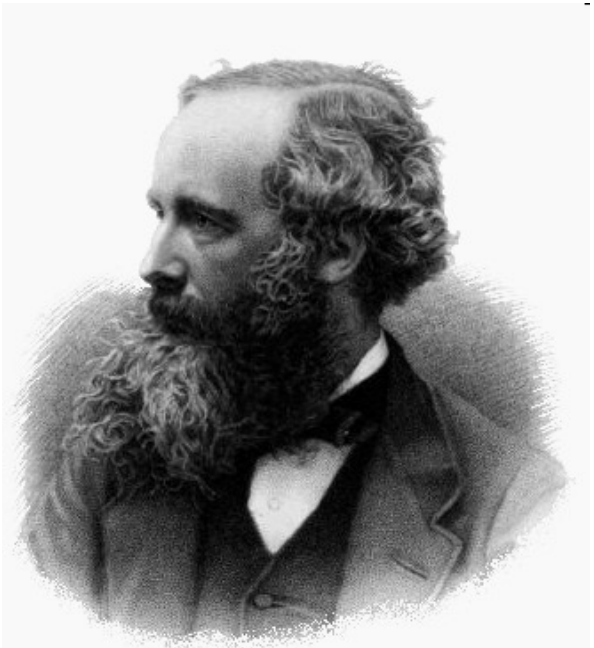

James Clerk Maxwell
(1831–1879)

$$\begin{cases} \nabla \cdot \mathbf{E} = \dfrac{\rho}{\epsilon_0} \\ \nabla \times \mathbf{E} = -\dfrac{\partial \mathbf{B}}{\partial t} \\ \nabla \cdot \mathbf{B} = 0 \\ \nabla \times \mathbf{B} = \mu_0 \mathbf{J} + \epsilon_0 \mu_0 \dfrac{\partial \mathbf{E}}{\partial t} \end{cases}$$

$x=2\pi r/\lambda$

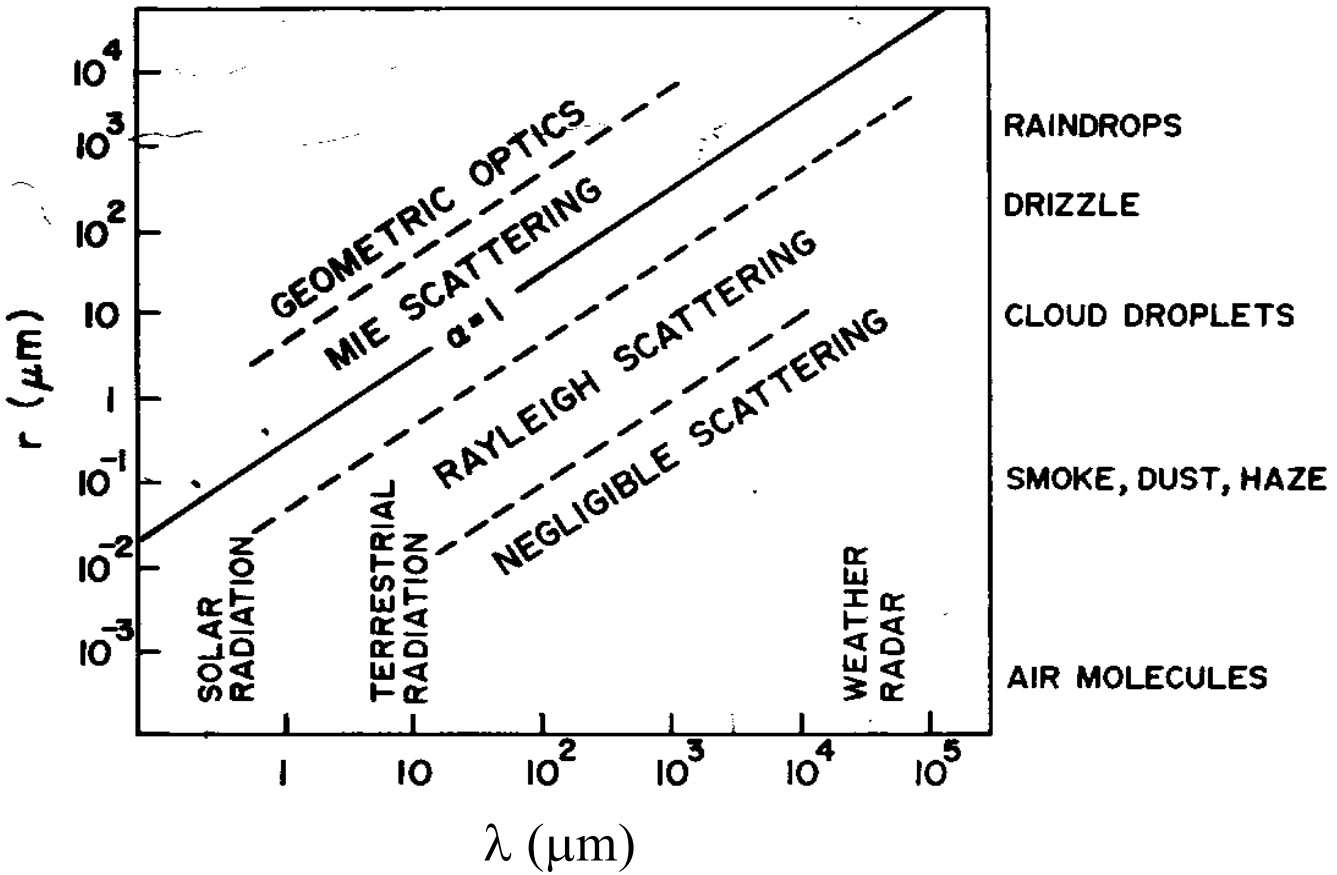

$$\begin{pmatrix} \mathrm{E}^{\parallel}{}_{d} \\ \mathrm{E}^{\perp}_{d} \end{pmatrix} = \begin{pmatrix} S_2(\theta) & S_3(\theta) \\ S_4(\theta) & S_1(\theta) \end{pmatrix} \frac{e^{-jkR}}{jkR} \begin{pmatrix} \mathrm{E}^{\parallel}_{i} \\ \mathrm{E}^{\perp}_{i} \end{pmatrix}$$

$$Q_{ext} = \frac{2}{x^2} \sum_{n=1}^{N} (2n+1)\mathrm{Re}(a_n + b_n), \tag{1a}$$

$$Q_{sca} = \frac{2}{x^2} \sum_{n=1}^{N} (2n+1)(|a_n|^2 + |b_n|^2), \tag{1b}$$

$$g = \frac{4}{x^2 Q_{sca}} \sum_{n=1}^{N} \left[\frac{n(n+2)}{n+1} \mathrm{Re}(a_n a_{n+1}^* + b_n b_{n+1}^*) + \frac{2n+1}{n(n+1)} \mathrm{Re}(a_n b_n^*) \right], \tag{1c}$$

$$S_1(\mu) = \sum_{n=1}^{N} \frac{2n+1}{n(n+1)} [a_n \pi_n(\mu) + b_n \tau_n(\mu)], \tag{1d}$$

$$S_2(\mu) = \sum_{n=1}^{N} \frac{2n+1}{n(n+1)} [a_n \tau_n(\mu) + b_n \pi_n(\mu)], \tag{1e}$$

which are, respectively, the extinction efficiency, scattering efficiency, asymmetry factor, and complex scattering amplitudes for two orthogonal directions of incident polarization.

($|S_1|^2$ and $|S_2|^2$ are the scattered intensities.)

$\pi_h(\cos\theta)$ and $\tau_h(\cos\theta)$ are obtained from $L_h(\cos\theta)$, which are h-order Legendre polynomials

$$Q^{est}(x,m) = \frac{\sigma_{est}}{\pi r^2} = \frac{2}{x^2}\sum_{h=1}^{\infty}(2h+1)\,\mathrm{Re}(a_h + b_h)$$

$$Q^{sc}(x,m) = \frac{\sigma_{sc}}{\pi r^2} = \frac{2}{x^2}\sum_{h=1}^{\infty}(2h+1)\left(|a_h|^2 + |b_h|^2\right)$$

$$Q^{sc}(x,m) = \frac{\sigma^{sc}}{\pi r^2} = c_1 x^4 (1 + c_2 x^2 + c_3 x^4 + \cdots)$$

If the imaginary part of the refractive index is zero:

$$c_1 = \frac{8}{3}\left(\frac{m^2-1}{m^2+2}\right)^2, \qquad c_2 = \frac{6}{5}\left(\frac{m^2-1}{m^2+2}\right)$$

The first order approximation gives the Rayleigh scattering

$$a_h(m,x) = \frac{\psi_h(x)\psi'_h(mx) - m\psi_h(mx)\psi'_h(x)}{\zeta_h(x)\psi'_h(mx) - m\zeta'_h(x)\psi_h(mx)}$$

$$b_h(m,x) = \frac{m\psi_h(x)\psi'_h(mx) - \psi_h(mx)\psi'_h(x)}{m\zeta_h(x)\psi'_h(mx) - \zeta'_h(x)\psi_h(mx)}$$

Mie scattering coefficients a_h e b_h are a combination of Riccati-Bessel functions ψ_h e ζ_h

65

$$N \sim x + 4\,x^{1/3} + 2$$

Wiscombe, 1980

$$Q_{ext}=\sigma_{ext}/(\pi r^2)$$

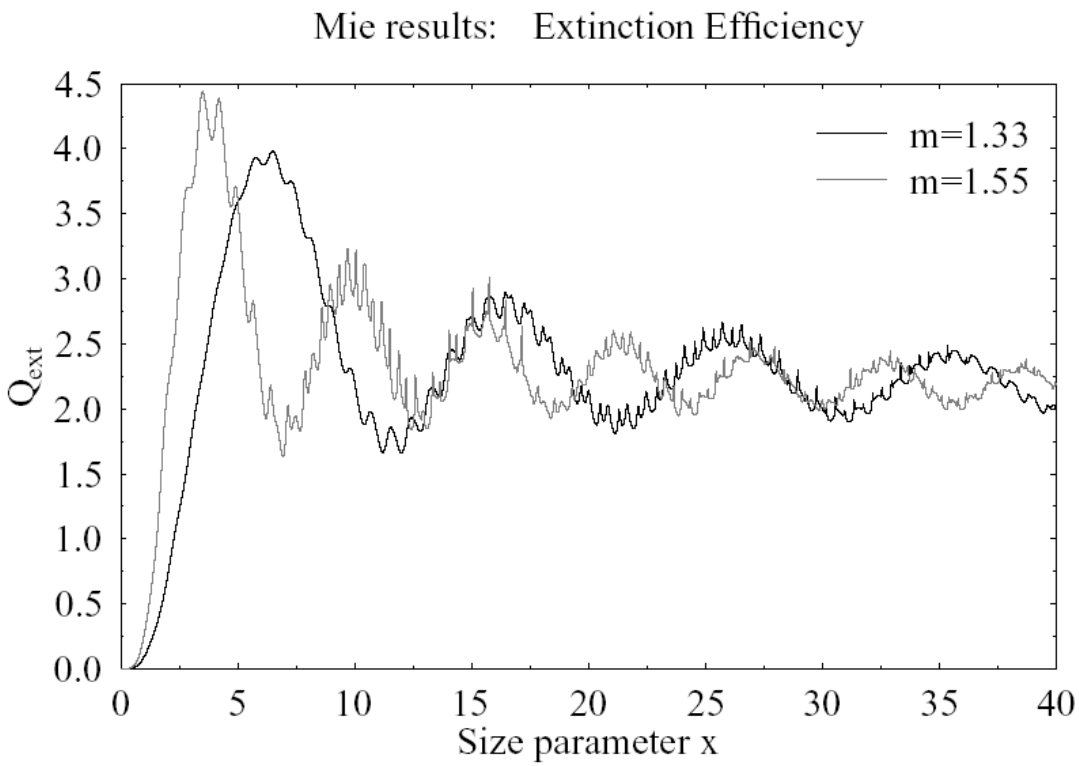

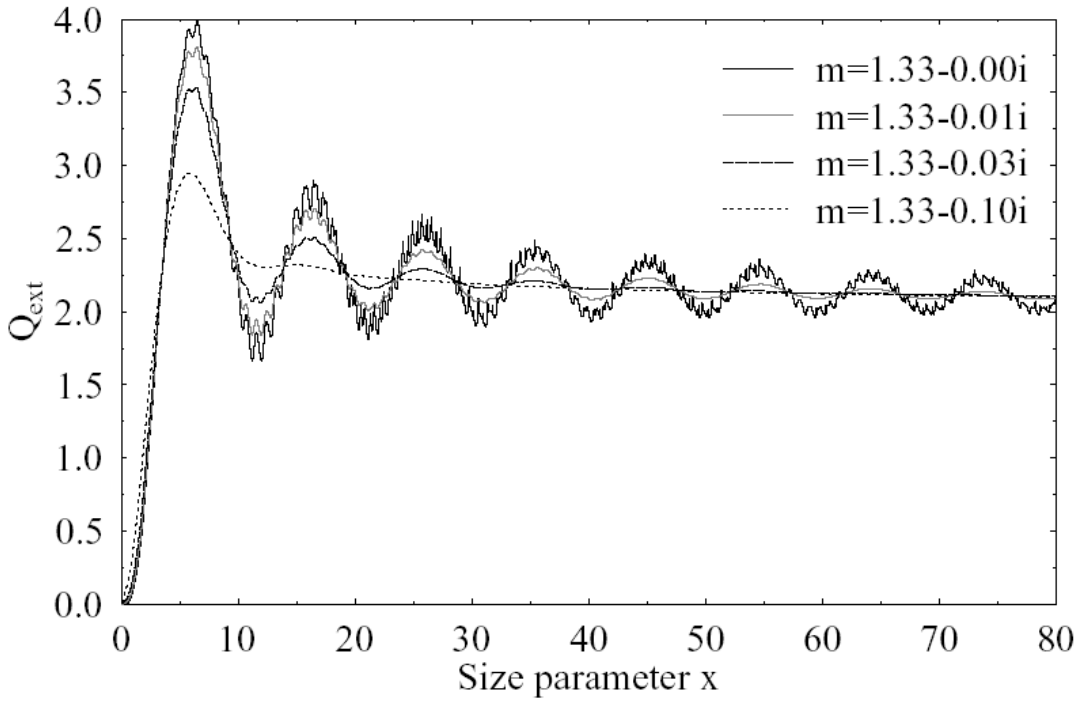
4.0
3.5
3.0
2.5
2.0
1.5
1.0
0.5
0.0
Q_{ext}
0
10
20
30
40
50
60
70
80
Size parameter x
m=1.33-0.00i
m=1.33-0.01i
m=1.33-0.03i
m=1.33-0.10i

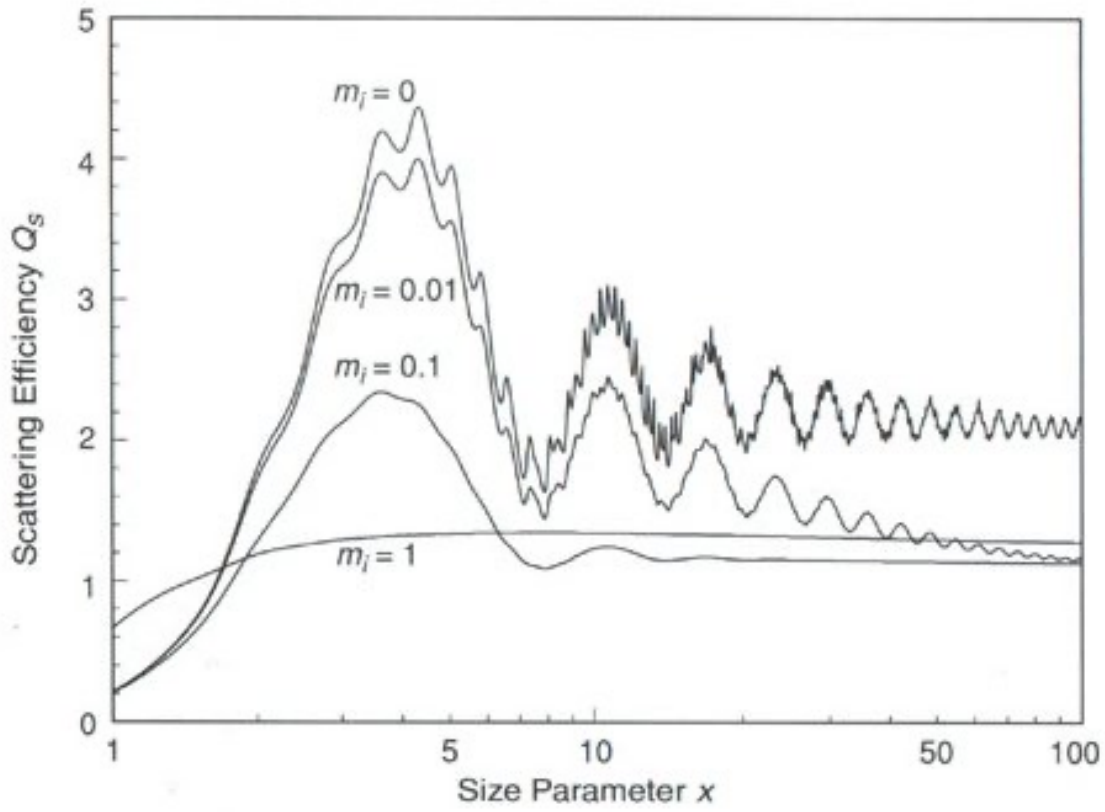
Scattering Efficiency Q_s
Size Parameter x
$m_i = 0$
$m_i = 0.01$
$m_i = 0.1$
$m_i = 1$
0
1
2
3
4
5
1
5
10
50
100

70

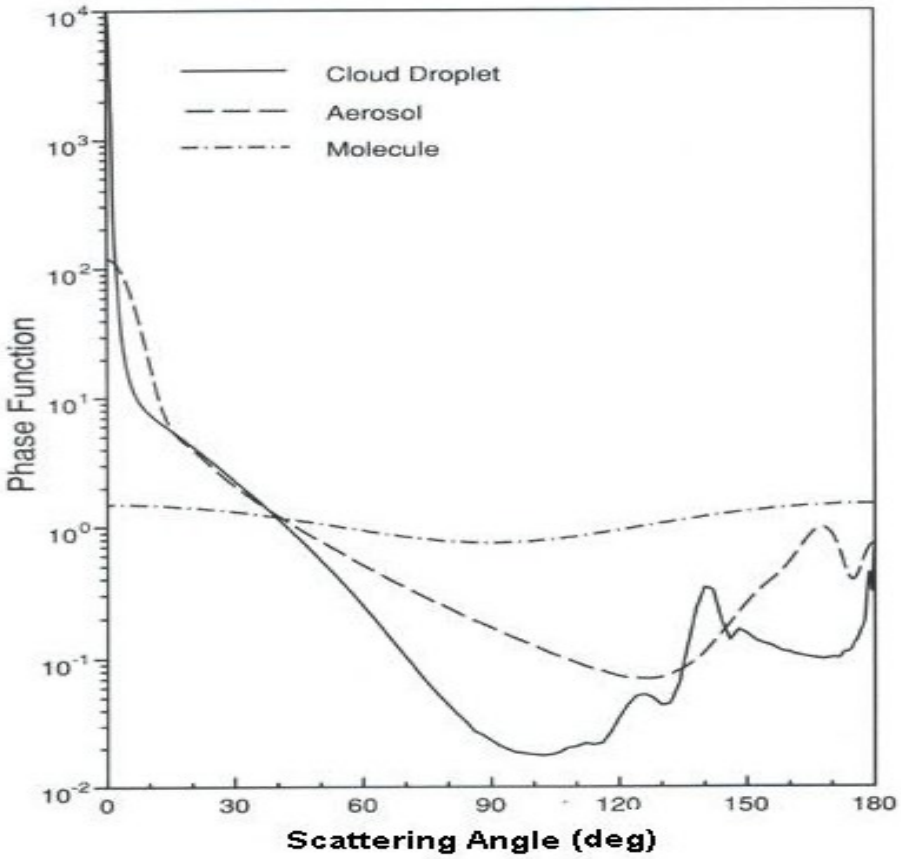
Cloud Droplet
Aerosol
Molecule
Phase Function
10^4
10^3
10^2
10^1
10^0
10^{-1}
10^{-2}
0
30
60
90
120
150
180
Scattering Angle (deg)

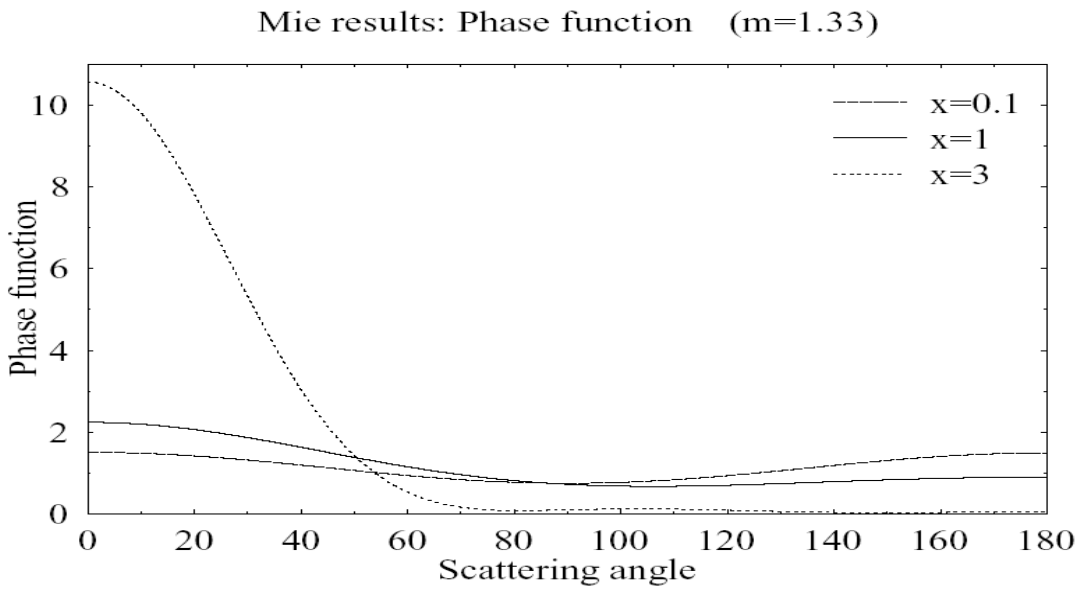
Mie results: Phase function (m=1.33)
Phase function
Scattering angle
x=0.1
x=1
x=3
0
2
4
6
8
10
0
20
40
60
80
100
120
140
160
180

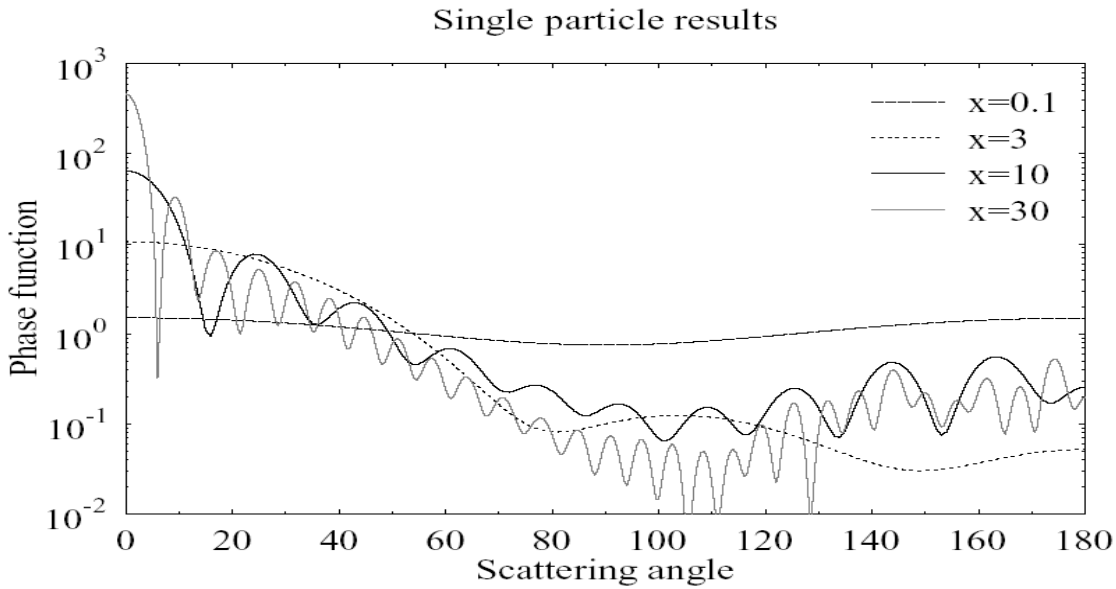
Single particle results
Phase function
Scattering angle
x=0.1
x=3
x=10
x=30
10^{3}
10^{2}
10^{1}
10^{0}
10^{-1}
10^{-2}
0
20
40
60
80
100
120
140
160
180

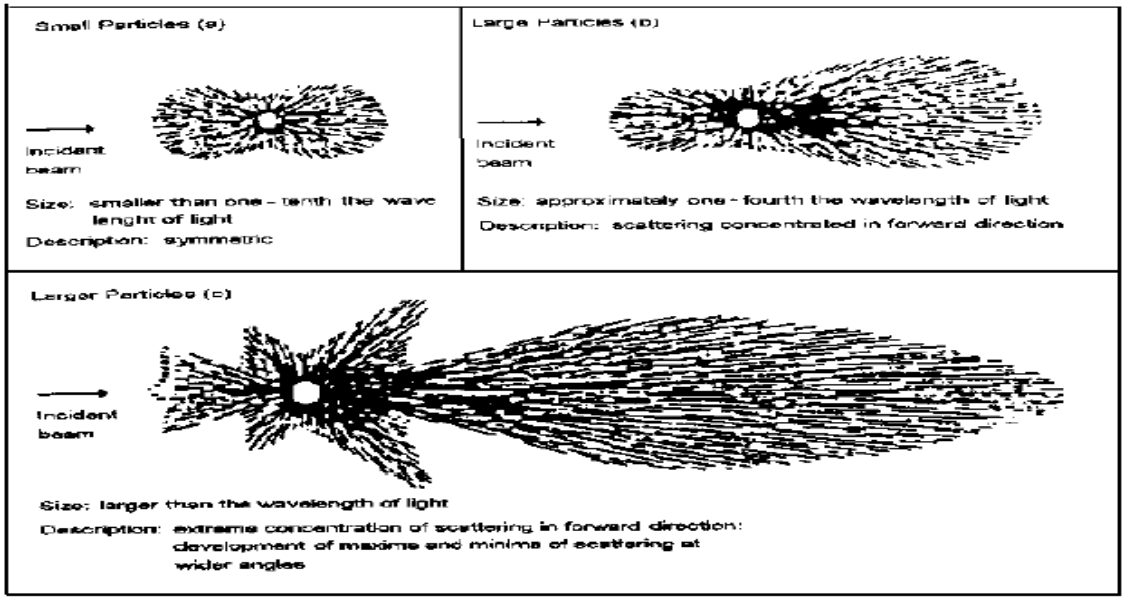

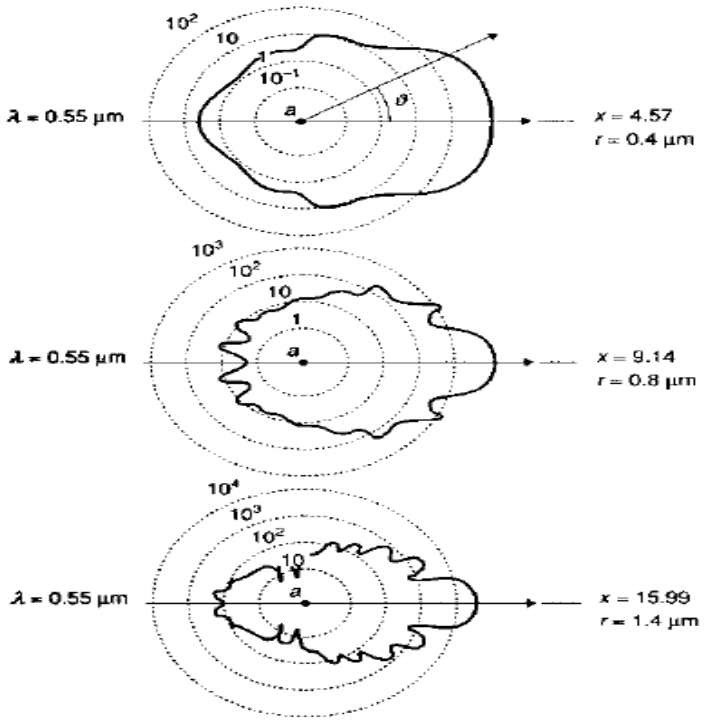

Fig. 6.3 - Diagrammi polari dell'intensità nel piano di diffusione per particelle **sferiche** *a* debolmente assorbenti, di raggio *r*, e per radiazione incidente non **polarizzata** di lunghezza d'onda λ=0.55 μm; $x=2\pi r/\lambda$, è il parametro di Mie.

THANKS!

IR0000032 – ITINERIS, Italian Integrated Environmental Research Infrastructures System
(D.D. n. 130/2022 - CUP B53C22002150006) Funded by EU - Next Generation EU PNRR-Mission 4 “Education and Research” - Component 2: “From research to business” - Investment 3.1: “Fund for the realisation of an integrated system of research and innovation infrastructures”

Finanziato dall'Unione europea NextGenerationEU
Ministero dell'Università e della Ricerca
Italiadomani